A K-BAND–SELECTED PHOTOMETRIC REDSHIFT CATALOG IN THE HUBBLE DEEP FIELD SOUTH: SAMPLING THE REST-FRAME V BAND TO z = 3[1]

GREGORY RUDNICK,[2] MARIJN FRANX,[3] HANS-WALTER RIX,[2,4] ALAN MOORWOOD,[5] KONRAD KUIJKEN,[6] LOTTIE VAN STARKENBURG,[3] PAUL VAN DER WERF,[3] HUUB RÖTTGERING,[3] PIETER VAN DOKKUM,[7] AND IVO LABBÉ[3]

ABSTRACT

We present the first results from the Faint Infra-Red Extragalactic Survey of the Hubble Deep Field South (HDF-S). Using a combination of deep near-infrared (NIR) data obtained with the Infrared Spectrograph and Array Camera at the VLT and the WFPC2 *Hubble Space Telescope* data, we construct a K-band–selected sample which is 50% and 90% complete for $K_{s,\mathrm{AB}} \leq 23.5$ and $K_{s,\mathrm{AB}} \leq 22.0$, respectively, where the magnitudes are measured over a 2″0 diameter aperture. For $z \leq 3$, our selection by the K-band flux chooses galaxies based on wavelengths redder than the rest-frame V band, and so selects them in a way that is less dependent on their current star formation rates than selection in the rest-frame UV. We developed a new photometric redshift technique that models the observed spectral energy distribution (SED) with a linear combination of empirical galaxy templates. We tested this technique using 150 spectroscopic redshifts in the Hubble Deep Field North (HDF-N) from the Cohen et al. sample (published in 2000) and found $\Delta z/(1 + z) \approx 0.07$ for $z < 6$. We show that we can derive realistic error estimates in z_{phot} by combining the systematic uncertainties derived from the HDF-N with errors in z_{phot}, which depend on the observed flux errors. We estimate photometric redshifts for 136 galaxies in the HDF-S from the full seven-band, 0.3–2.2 μm SED. In finding the correct z_{phot}, our deep NIR data is important for breaking the redshift degeneracy between templates of identical observed optical colors. The redshift histogram of galaxies in the HDF-S shows distinct structure with a sharp peak at $z \approx 0.5$ and a broad enhancement at $z \sim 1$–1.4. We find that 12% of our galaxies with $K_{s,\mathrm{vega}} < 21$ lie at $z \geq 2$. While this is higher than the fraction predicted in $\Omega_M = 1$ hierarchical models of galaxy formation, we find that published predictions using pure luminosity evolution models produce too many bright galaxies at redshifts greater than unity. Finally, we use our broad wavelength coverage to measure the rest-frame UBV luminosities, L^{rest}, for $z \leq 3$. There is a paucity of galaxies brighter than $L_V^{\mathrm{rest}} \geq 1.4 \times 10^{10}\ h^{-2}\ L_{\odot}$ at $z \sim 1.5$–2, similar to what Dickinson found for the HDF-N (published in 2001). However, z_{phot} is particularly uncertain in this regime, and spectroscopic confirmation is required. We also note that at $z > 2$ we find very luminous galaxies with $L_V^{\mathrm{rest}} \geq 5 \times 10^{10}\ h^{-2}\ L_{\odot}$ (for $\Omega_M = 0.3$, $\Omega_{\Lambda} = 0.7$, and $H_0 = 100\ h$ km s^{-1} Mpc^{-1}). Local B-band luminosity functions predict 0.1 galaxies in the redshift range $2 \leq z \leq 3.5$ and with $L_B^{\mathrm{rest}} \geq 5 \times 10^{10}\ h^{-2}\ L_{\odot,B}$, but we find nine. The discrepancy can be explained if L_B^* increases by a factor of 2.4–3.2 with respect to locally determined values. Random errors in the photometric redshift can also play a role, and spectroscopic confirmation of the redshifts of these bright galaxies is required.

Key words: galaxies: distances and redshifts — galaxies: evolution — galaxies: formation — galaxies: high-redshift — galaxies: photometry

1. INTRODUCTION

Observational constraints on galaxy formation have improved dramatically in recent years, as large, ground-based telescopes, the *Hubble Space Telescope* (*HST*), and high-efficiency, wide-field instruments have allowed astronomers, for the first time, to identify and observe statistically significant samples of high-redshift galaxies. With these data, one can address several important questions: What is the cosmic star formation history (SFH; see, e.g., Lilly et al. 1996; Madau et al. 1996)? What is the mean stellar age of galaxies as a function of redshift and color (Papovich, Dickinson, & Ferguson 2001)? What is the role of dust in galaxy spectral energy distributions (SEDs; see, e.g., Thompson, Weymann, & Storri-Lombardi 2001; Adelberger & Steidel 2000; Mobasher & Mazzei 2000)? What are the sizes and luminosities of galaxies as a function of redshift and color (see, e.g., Giallongo et al. 2000; Poli et al. 1999; Lilly et al. 1998; Schade et al. 1996)? What are the SFHs of galaxies with different morphologies (Brinchmann & Ellis 2000)?

The most efficient method to date for detecting and confirming high-redshift galaxies is the Lyman break (LB) technique originally developed by Steidel & Hamilton (1992). Photometric preselection by this method, followed by spectroscopic confirmation at the Keck I and II telescopes, has resulted in the discovery of ~900 galaxies at $z \gtrsim 2.5$ (see,

e.g., Steidel et al. 1996, 1999). Although a powerful tool, this method has two intrinsic limitations: it is sensitive only to unobscured galaxies with a high current star formation rate (SFR), and it can only find galaxies beyond $z \gtrsim 2.3$.

A general method for estimating galaxy redshifts from broadband photometry is the photometric redshift technique (see, e.g., contributions in Weymann et al. 1999), of which the LB technique is a special case. Connolly et al. (1995) demonstrated for galaxies with $z \lesssim 1$ that accurate and reliable photometric redshifts ($\langle |z_{\rm spec} - z_{\rm phot}| \rangle \sim 0.05$) could be obtained if a "training set" with spectroscopic redshifts was available. When large spectroscopically confirmed samples with identical photometry are not available, template fitting can provide alternative redshift estimates (see, e.g., Benítez 2000; Csabai et al. 2000; Fernández-Soto, Lanzetta, & Yahil 1999, hereafter FLY99; Fontana et al. 1999, hereafter F99; Pascarelle, Lanzetta, & Fernández-Soto 1998; Giallongo et al. 1998; Sawicki, Lin, & Yee 1997; Gwyn & Hartwick 1996). There, the most likely redshift for a galaxy is obtained by comparing multiband observed colors with the expected colors of redshifted templates. With an appropriate choice of templates—empirical, synthetic, or both—this method allows an accurate redshift determination across a wide range in z and independent of the SFH. As with the LB technique, however, all photometric methods rely on features in the SED to pin down the redshift. Beyond $z \approx 1$, the calcium H and K "4000 Å" break and the Balmer break are moved into the near-infrared (NIR), while the LB still falls blueward of the atmospheric UV cutoff until $z \approx 2.3$. To identify galaxies in the important redshift range $1 \lesssim z \lesssim 2.3$, we need to rely on rest-frame optical breaks and hence require deep NIR imaging. Such NIR data can also detect the LB at very high redshifts ($z \gtrsim 10$).

J-, H-, and K-band fluxes also allow us to select galaxies at $z \leq 3$ based on their rest-frame V-band light. Such a selection is less biased toward galaxies with high SFRs than a flux-limited selection in the rest-frame UV. Indeed, at the present time, NIR selection is the best practical way to select galaxies by their stellar mass. As shown by Kauffmann & Charlot (1998, hereafter KC98), the redshift distribution for a sample selected by stellar mass can serve as a powerful constraint on theories of galaxy formation. KC98 used semianalytic models, coupled with stellar population synthesis codes, to predict the redshift distribution in K-band–selected samples of differing flux limits. They found that a generic prediction of hierarchical models is a lack of K-band luminous galaxies at high redshift.

We initiated the Faint Infra-Red Extragalactic Survey (FIRES; Franx et al. 2000) at the VLT (Labbé et al. 2001) to access rest-frame optical wavelengths over a large range in redshift. This public data set combines some of the deepest optical images from HST with very deep ground-based J_s HK_s data from the Infrared Spectrograph and Array Camera (ISAAC; Moorwood 1997) at the VLT. Once complete, this survey will have accumulated ≈ 192 hr of time with the ISAAC instrument and ≈ 8 hr of FORS1/2 time to obtain imaging of both the WFPC2 field of the HDF-S and a mosaic of six WFPC2 fields covering the $z = 0.83$ cluster MS 1054-03. In conjunction with the HST data, this provides seven-band photometry over an area of ≈ 31 arcmin^2. Our unique data set, coupled with an accurate photometric redshift technique, will allow us to directly trace the mass assembly of galaxies regardless of their SFH through a flux-

limited selection in the K band. Using the redshifts and the observed SEDs, we can then reconstruct the rest-frame SEDs of galaxies over a large range in intrinsic luminosity and rest-frame color.

In this paper, we present initial results from observations the HDF-S obtained as part of FIRES. With these data, we derive photometric redshifts with accompanying uncertainties and determine the rest-frame U-, B-, and V-band luminosities for galaxies with $z \leq 3$ in a K_s-band–selected sample. Our current data are deep enough to probe galaxies at $z = 2$ with rest-frame luminosities, $L^{\rm rest} \geq 10^{10} L_\odot$. With our data, we place new constraints on the redshift distribution in the HDF-S for $1 < z < 2.5$. In § 2, we present the observations and data. In § 3, we discuss our new photometric redshift technique, including a discussion of its reliability. We show and discuss the redshift distribution of our sample and the $L^{\rm rest}$ values of our galaxies in § 4. We summarize in § 5. We adopt a Λ cosmology throughout the paper with $\Omega_M = 0.3$, $\Omega_\Lambda = 0.7$, and $H_0 = 100$ km s^{-1} Mpc^{-1}. If h is omitted, assume $h = 1.0$.

2. OBSERVATIONS AND DATA

2.1. Observations

We present the first data taken on the HDF-S in the fall of 1999. The total exposure times were 6.7, 5.7, and 7.5 hr in J_s, H, and K_s, respectively. The field was centered at $22^{\rm h}32^{\rm m}55^{\rm s}.03$, $60°33'09''.8$ (J2000). All these data were taken in service mode at the Antu telescope on the nights of 1999 October 21–29, 1999 November 19, and 1999 December 18–19, before its primary mirror was recoated. Despite the reduced sensitivity, the data were of exceptional quality. Most of the nights had excellent seeing in all bands, and the combined images had a median image quality of $0''.55$ (J_s band), $0''.50$ (H band), and $0''.50$ (K_s band). ISAAC has a pixel scale of $0''.147$ pixel^{-1} and a field of almost $150'' \times 150''$, which almost perfectly matches the size of the WFPC2 field.

Our observing strategy followed established procedures for ground-based NIR work. We dithered the images randomly in a $20''.0$ box to allow the construction of sky frames with minimal object contamination. This works well for a field such as the HDF-S, which contains no large, bright objects. Our exposure times were 120, 120, and 60 s split into four, six, and six integrations for J_s, H, and K_s, respectively.

For our optical data, we used the version 2 (Casertano et al. 2000), reduced and calibrated F300W, F450W, F606W, and F814W WFPC2 data from the HDF-S.

2.2. Data Reduction

We reduced our ground-based images with IRAF[8] using the DIMSUM[9] package within IRAF and ECLIPSE.[10] We give a brief summary of our data reduction below. For further details, see the presentation of our full data set

---

(Labbé et al. 2001). For each individual science exposure in a given observing block (OB), a sky image was constructed from a maximum of eight temporally adjacent images and subtracted from the science frame. Cosmic rays were identified from the individual sky-subtracted frames, and all the sky-subtracted frames in a given OB were then aligned and combined. DIMSUM created a mask marking all pixels belonging to objects by applying a threshold to the combined image. Sky subtraction and cosmic-ray identification were repeated for the individual frames using the newly created object mask to exclude object pixels. We modified DIMSUM to account for the time-dependent bias in the ISAAC frames by subtracting the median on a line-by-line basis, excluding from the median calculation all object pixels in the object mask. The sky-subtracted frames were then flat-fielded before the final registration and combination. The flat-field images were created from a time sequence of twilight sky images using the ECLIPSE software. Individual frames for a given OB were registered and added together using the IMCOMBINE task in IRAF. The NIR images from all OBs for a given filter were then combined into a total image. Finally, we applied the documented geometric distortion correction to the combined image while simultaneously interpolating the final NIR images to 4 times the WFPC2 pixel scale ($0\farcs159$ pixel^{-1}).

A weight map was constructed for each NIR passband to reflect the exposure time at every pixel and, hence, the noise. For the *HST* data, we used the weight maps publicly distributed along with the science frames. These weight maps were used in all subsequent detection and photometry steps.

2.3. *Photometric Calibration*

Magnitude zero points were derived from standard star observations taken as part of the normal VLT calibration routine. For each standard star in each filter and on each night, we measured the flux in a circular aperture of radius $\sim 3''$ (20 pixels) and used the magnitude of that star, as given in Persson et al. (1998), to establish our zero point for that star. We derived a nightly zero point by combining all standard star observations in a given night and filter. By comparing these derived nightly zero points to the median zero points over all nights, we identified nonphotometric nights. We used the mean of the zero points on the photometric nights to determine the zero point for each bandpass. The uncertainties in the final zero points were ~ 0.02. Using these zero points, we derived the magnitudes of bright stars in the field for the OBs on the photometric nights, and used them to calibrate the final combined and distortion corrected image. All magnitudes in this paper are given in the AB system unless stated explicitly otherwise. For the NIR data, the adopted transformations from the Vega system to the AB system are taken from Bessell & Brett (1988; $J_{s,\,\mathrm{vega}} = J_{s,\,\mathrm{AB}} - 0.90$, $H_{\mathrm{vega}} = H_{\mathrm{AB}} - 1.37$, $K_{s,\mathrm{vega}} = K_{s,\,\mathrm{AB}} - 1.88$).

In our final reduced images, the 10 σ magnitude limits in a $2\farcs0$ circular aperture are $m_{\mathrm{AB}} = 23.8, 23.0,$ and 23.2 in J_s, H, and K_s, respectively. The 3 σ limits are $m_{\mathrm{AB}} = 25.1, 24.4,$ and 24.5. Our data are $\sim 0.25, 0.1,$ and 0.2 mag deeper in J_s, H, and K_s, respectively, than the data on the HDF-N taken at the Kitt Peak 4 m with the IRIM camera in April of 1996 (Dickinson 2001a). The F110W and F160W HDF-N NICMOS data (Dickinson 2001b) goes 1.1 and 1.9 mag deeper, respectively, than our J_s and H data. In the HDF-S our data are $\sim 1, 2.1,$ and 2.1 mag deeper in J_s, H, and K_s,

respectively, than the ESO Imaging Survey data from da Costa et al. (2001).

2.4. *Object Detection and Photometry*

Our first goal is to construct a K_s-band flux-limited catalog of objects. We used the SExtractor software (Bertin & Arnouts 1996) to detect objects from the final K_s image, using the K_s-band weight image. Faint objects are detected against a noisy background after convolving the image with a kernel representing the typical expected object size. Because SExtractor allows only one convolution kernel per detection pass, we must optimize the detection for a particular object size, biasing ourselves against faint objects of very different sizes. We choose a $0\farcs48$ FWHM Gaussian convolution kernel, extending over $0\farcs8 \times 0\farcs8$, which represents the size of the seeing disk. As in all deep surveys, deblending of overlapping or close object pairs is difficult and, to some extent, subjective. An ideal deblending algorithm will not "oversplit" single galaxies with knotty internal structure, but will split close groupings of separate galaxies. We settled on a single set of deblending parameters that nearly eliminate the oversplitting of galaxies: DEBLEND_NTHRESH = 32, DEBLEND_MINCONT = 0.0002. These parameters set the number of deblending subthresholds and the minimum contrast needed to deblend two objects, respectively.

To obtain consistent photometry across the full seven bands, we need to account for the vastly different pixel scales and resolutions between our space-based and ground-based images. To this end, we first resampled all the data to the same pixel scale, fitted the point-spread function in the NIR images with a double Gaussian, whose equally weighted components have FWHM = $0\farcs38$ and FWHM = $0\farcs75$, respectively, and convolved this with the optical data. To measure colors over identical angular scales in each band, we choose to measure the fluxes of all objects in a fixed $2\farcs0$ diameter aperture, whose position was chosen from the K_s-band image. For the largest objects, this aperture misses some flux, but this choice lessens the chance of measuring flux from two separate objects. Still, there are six pairs of objects whose $2\farcs0$ apertures overlap (identifications are 98, 99; 117, 127; 187, 188; 354, 364; 372, 373; and 397, 398). For some of these objects, the flux measurements of the galaxy might be strongly affected by the light from its nearest neighbor. In calculating the flux errors in all the images, we used the weight images discussed in (§ 2.2).

We used SExtractor to detect objects, using a detection threshold of 0.8 times the standard deviation of the background. The relative strength of the background at each pixel was given by the K_s-band weight image. For an object to enter the initial catalog, we required that a minimum of five contiguous pixels lie above the detection threshold. From the resulting initial catalog of 615 objects detected in the K_s-band image, we constructed a catalog optimized for photometric redshift estimates based on three criteria. (1) To homogenize the data quality, the value of the exposure time weight must exceed 0.5 and 0.25 for the VLT and *HST* images, respectively (this cut reduces our total usable image area to 4.3 arcmin^2). (2) To differentiate between stars and galaxies, we examined the FWHM and magnitude of objects in the F814W image. Objects were identified as stars if they satisfied either of the following two criteria: FWHM < 6 pixels and F814W$_{\mathrm{AB}}$ < 27 or FWHM < 15 pixels and F814W$_{\mathrm{AB}}$ < 22. The second of these criteria was

used to eliminate saturated stars. (3) To limit ourselves to magnitudes where the completeness is greater than 50%, we require that the object must have a total magnitude (the "AUTO" magnitude from SExtractor with a minimum 2″.0 diameter) of $K_{s,\mathrm{AB}}^{\mathrm{tot}} \leq 23.5$, roughly a 6 σ detection (see § 2.5). The exposure time criterion reduced the initial catalog to 316 objects, and the removal of all point sources in the F814W image left 293. Of these, 136 objects had $K_{s,\mathrm{AB}}^{\mathrm{tot}} \leq 23.5$ and were entered into our final catalog (see Table 1). The K_s-band image is shown in Figure 1, along with all 136 objects and their identification numbers from the final catalog. All flux measurements are summarized in Table 1.

2.5. Completeness

The issue of completeness must be addressed in every survey for faint, extended objects. The detectability of an object depends not only on its apparent magnitude, but also on its morphology and mean surface brightness. The detection algorithm used by SExtractor looks for continuously connected pixels above a certain threshold with respect to the background. Relatively bright objects of low surface brightness may be missed by this technique. To understand our detection completeness, we added objects to the K_s-band image and then determined how successful we were at detecting them. We constructed three different types of model objects: an elliptical galaxy with a de Vaucouleurs profile and an axis ratio of $b/a = 0.7$ and two exponential galaxies with $b/a = 0.4$ and $b/a = 0.8$. For each of these three profile types, we made a magnitude grid of $K_{s,\mathrm{AB}} = 20$,

21, 22, 23, 24, and 25 and a size grid of $R_H = 0″.25, 0″.5, 0″.8$, and $1″.6$, where R_H is the half-light radius. For each profile type, magnitude, and size, we convolved the synthetic galaxy images with the seeing (see § 2.4) and inserted about 50 such objects into the K_s image at simple grid positions. We then ran SExtractor on the new image and counted how many of the model objects were detected for each set of parameters and how well these parameters (apparent magnitude and size) were recovered. Figure 2a shows how the completeness depends on surface brightness, parameterized by both input magnitude and size, for a given profile shape and axial ratio. For a fixed size, Figure 2b shows how little completeness changes with profile shape.

To asses the actual 50% completeness limit for our sample, we must select size parameters most applicable to galaxies near our flux limit. To map the input sizes used in Figure 2 to the sizes returned by SExtractor for the model images, we compared, for different magnitudes, R_H to

$$R_{\mathrm{out}} = \sqrt{R_{\mathrm{kron}}^2 - R_{\mathrm{seeing}}^2} \ . \qquad (1)$$

Here R_{kron} is the Kron radius (Kron 1980) calculated by SExtractor, and R_{seeing} is the FWHM/2 of the actual observations. At the faintest level where we could both retrieve the input magnitude and also see a defined relation between input and output size ($K_{s,\mathrm{AB}} \sim 22$), we measured that objects had a typical R_{kron} of $0″.6$. Using our input-output size relations averaged over profile type, we associated this measured radius with an intrinsic R_H of $0″.8$. As a choice of profile type, we conservatively chose the curve for which we
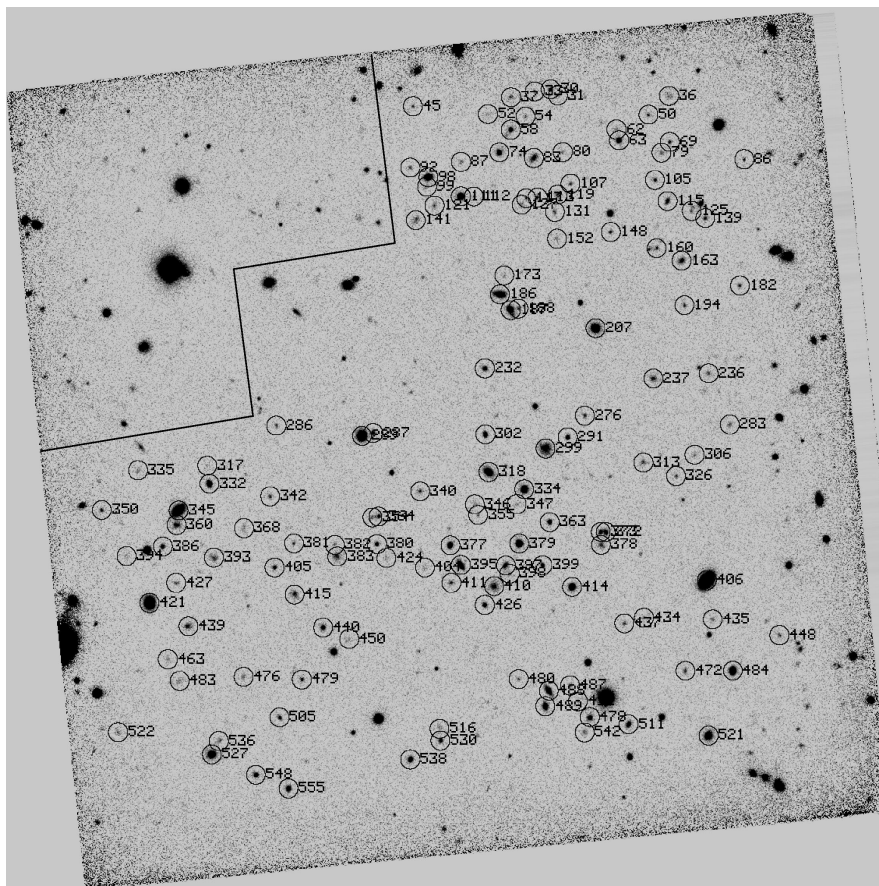

Fig. 1.—Reduced K_s-band image. All 136 objects in the final catalog are marked, and the numbers are the identification numbers in the catalog shown in Table 1. The outline of the WFPC2 field of the HDF-S is shown.

TABLE 1
PHOTOMETRIC CATALOG

ID	F300W[a]	F450W[a]	F606W[a]	F814W[a]	J_s[a]	H[a]	K_s[a]	K_s^{tot}[b]
HDFS 1-30	17.5 ± 2.0	62.4 ± 1.0	81.7 ± 0.7	140.4 ± 1.2	465.8 ± 15.2	528.4 ± 29.2	629.7 ± 24.8	700.4 ± 39.6
HDFS 1-33	19.2 ± 1.9	37.6 ± 1.0	45.2 ± 0.7	93.9 ± 1.2	128.3 ± 15.1	195.7 ± 29.0	184.7 ± 24.7	186.5 ± 24.5
HDFS 1-31	6.9 ± 1.9	11.7 ± 1.0	21.9 ± 0.6	41.1 ± 1.2	71.1 ± 14.1	119.7 ± 27.4	184.1 ± 23.1	261.5 ± 38.4
HDFS 1-36	0.3 ± 2.0	34.9 ± 1.0	73.8 ± 0.7	90.5 ± 1.2	119.4 ± 13.5	275.2 ± 26.2	337.0 ± 22.0	353.4 ± 28.0
HDFS 1-37	4.6 ± 2.0	1.0 ± 1.0	3.5 ± 0.7	6.2 ± 1.2	11.3 ± 14.7	119.1 ± 28.3	281.7 ± 24.0	337.1 ± 37.1
HDFS 1-45	1.9 ± 2.0	1.4 ± 1.0	9.6 ± 0.7	71.4 ± 1.2	228.4 ± 14.7	225.4 ± 28.4	216.9 ± 24.1	201.1 ± 22.4
HDFS 1-50	0.3 ± 1.9	2.0 ± 1.0	5.4 ± 0.7	18.3 ± 1.2	132.0 ± 12.4	247.2 ± 23.6	294.2 ± 19.9	289.0 ± 20.2
HDFS 1-52	30.9 ± 1.9	53.8 ± 1.0	60.1 ± 0.6	85.1 ± 1.2	139.0 ± 13.4	151.8 ± 25.9	146.9 ± 21.8	174.4 ± 26.5
HDFS 1-54	16.2 ± 1.9	23.5 ± 1.0	31.6 ± 0.6	52.4 ± 1.2	98.0 ± 13.0	127.7 ± 24.9	159.0 ± 21.1	150.8 ± 28.7
HDFS 1-62	7.7 ± 1.9	28.6 ± 0.9	37.3 ± 0.6	75.3 ± 1.2	131.4 ± 11.3	140.9 ± 21.6	220.0 ± 18.2	230.4 ± 29.9
HDFS 1-58	4.3 ± 1.9	4.3 ± 1.0	17.5 ± 0.6	75.1 ± 1.2	388.1 ± 12.1	576.8 ± 23.1	782.9 ± 19.5	858.8 ± 29.7
HDFS 1-63	62.9 ± 1.9	124.9 ± 0.9	287.9 ± 0.6	491.4 ± 1.2	823.6 ± 11.5	986.8 ± 22.0	1179.9 ± 18.5	1255.0 ± 26.3
HDFS 1-69	22.3 ± 1.9	32.6 ± 0.9	46.6 ± 0.6	92.8 ± 1.2	193.9 ± 11.5	248.7 ± 22.0	308.5 ± 18.5	294.5 ± 18.2
HDFS 1-74	8.9 ± 1.9	22.0 ± 0.9	51.7 ± 0.6	166.1 ± 1.2	536.9 ± 11.5	858.4 ± 22.0	1248.0 ± 18.5	1349.0 ± 26.6
HDFS 1-79	25.2 ± 1.9	83.7 ± 0.9	99.7 ± 0.6	120.1 ± 1.2	211.8 ± 11.5	236.9 ± 22.0	249.8 ± 18.5	306.6 ± 28.0
HDFS 1-80	-0.3 ± 1.9	23.6 ± 0.9	44.2 ± 0.6	57.0 ± 1.2	80.2 ± 11.5	63.5 ± 22.0	165.0 ± 18.5	153.0 ± 17.2
HDFS 1-83	103.7 ± 1.9	163.8 ± 0.9	338.9 ± 0.6	534.6 ± 1.2	739.3 ± 11.5	784.4 ± 22.0	896.1 ± 18.5	1087.8 ± 30.1
HDFS 1-86	14.4 ± 3.1	93.2 ± 1.2	177.8 ± 0.9	256.5 ± 1.7	308.0 ± 13.0	312.9 ± 24.5	184.1 ± 20.6	188.3 ± 22.1
HDFS 1-87	2.0 ± 1.9	5.4 ± 1.0	12.3 ± 0.6	19.4 ± 1.2	83.6 ± 11.5	79.6 ± 22.1	196.8 ± 18.6	187.0 ± 18.0
HDFS 1-92	8.3 ± 2.0	16.7 ± 1.0	24.7 ± 0.7	41.4 ± 1.2	134.6 ± 11.5	216.8 ± 22.0	231.2 ± 18.5	216.0 ± 17.2
HDFS 1-98	2.3 ± 2.0	38.6 ± 1.0	221.7 ± 0.6	846.6 ± 1.2	2035.4 ± 11.5	2785.0 ± 22.0	3513.2 ± 18.5	3620.1 ± 26.7
HDFS 1-105......	-3.6 ± 1.9	3.1 ± 0.9	2.1 ± 0.6	7.5 ± 1.2	45.4 ± 11.5	235.4 ± 22.0	368.2 ± 18.6	363.0 ± 19.5
HDFS 1-107......	34.3 ± 1.9	48.0 ± 0.9	60.6 ± 0.6	101.8 ± 1.2	156.7 ± 11.5	232.0 ± 22.0	195.1 ± 18.5	181.0 ± 17.2
HDFS 1-99	16.1 ± 1.8	27.7 ± 0.9	44.1 ± 0.6	89.5 ± 1.1	145.3 ± 10.6	152.6 ± 20.3	180.7 ± 17.1	203.9 ± 26.5
HDFS 1-119......	35.4 ± 1.9	50.4 ± 0.9	75.9 ± 0.6	166.4 ± 1.2	304.0 ± 11.5	305.8 ± 22.0	339.7 ± 18.5	354.3 ± 21.8
HDFS 1-111......	7.0 ± 1.9	50.8 ± 0.9	251.3 ± 0.6	802.5 ± 1.2	1931.8 ± 11.5	2662.9 ± 22.0	3228.2 ± 18.5	3267.8 ± 26.2
HDFS 1-112......	15.2 ± 1.9	43.8 ± 0.9	52.8 ± 0.6	64.5 ± 1.2	131.9 ± 11.4	183.6 ± 22.0	153.4 ± 18.5	157.2 ± 30.2
HDFS 1-113......	-2.1 ± 1.9	11.2 ± 0.9	21.1 ± 0.6	38.7 ± 1.2	186.3 ± 11.5	218.6 ± 22.0	354.2 ± 18.5	342.4 ± 20.0
HDFS 1-117......	5.8 ± 1.9	5.8 ± 0.9	6.2 ± 0.6	12.9 ± 1.2	57.5 ± 11.4	148.6 ± 21.9	183.8 ± 18.5	170.4 ± 17.1
HDFS 1-115......	22.6 ± 1.9	49.8 ± 0.9	114.4 ± 0.6	228.3 ± 1.2	373.3 ± 11.5	470.6 ± 22.0	568.7 ± 18.6	564.2 ± 22.5
HDFS 1-127......	25.7 ± 1.9	38.5 ± 0.9	55.5 ± 0.6	113.3 ± 1.2	147.7 ± 11.5	129.4 ± 22.0	192.0 ± 18.5	276.3 ± 35.2
HDFS 1-121......	48.4 ± 2.0	63.8 ± 1.0	117.0 ± 0.6	181.6 ± 1.2	228.9 ± 11.5	204.1 ± 22.1	256.1 ± 18.6	276.5 ± 21.9
HDFS 1-125......	1.8 ± 1.8	7.2 ± 0.9	11.8 ± 0.6	23.5 ± 1.1	99.5 ± 10.5	131.5 ± 20.1	179.3 ± 16.9	178.7 ± 23.6
HDFS 1-131......	5.2 ± 1.9	19.0 ± 0.9	28.0 ± 0.6	45.7 ± 1.2	141.8 ± 11.5	179.4 ± 22.0	244.3 ± 18.5	233.5 ± 19.7
HDFS 1-139......	5.1 ± 1.9	38.5 ± 1.0	54.9 ± 0.6	77.7 ± 1.2	226.1 ± 11.5	294.4 ± 22.0	395.2 ± 18.5	393.3 ± 26.0
HDFS 1-141......	72.3 ± 1.9	103.2 ± 1.0	183.8 ± 0.7	293.6 ± 1.2	381.5 ± 11.5	353.1 ± 22.0	440.7 ± 18.5	577.6 ± 29.6
HDFS 1-148......	-4.1 ± 1.9	2.0 ± 0.9	3.8 ± 0.6	9.6 ± 1.2	79.8 ± 11.5	191.7 ± 22.0	244.4 ± 18.6	226.6 ± 17.2
HDFS 1-152......	-1.9 ± 1.9	11.1 ± 0.9	31.4 ± 0.6	40.7 ± 1.2	70.6 ± 11.5	171.0 ± 22.0	176.0 ± 18.5	219.0 ± 26.6
HDFS 1-160......	2.5 ± 1.9	97.1 ± 0.9	150.4 ± 0.6	176.0 ± 1.1	199.7 ± 11.1	286.4 ± 21.4	365.2 ± 18.0	356.9 ± 22.1
HDFS 1-163......	11.3 ± 1.9	42.2 ± 0.9	55.6 ± 0.6	106.4 ± 1.2	402.9 ± 11.5	601.6 ± 22.0	781.1 ± 18.5	812.1 ± 26.3
HDFS 1-173......	19.0 ± 1.9	29.0 ± 0.9	32.9 ± 0.6	52.9 ± 1.2	106.4 ± 11.5	88.8 ± 22.0	148.9 ± 18.5	182.9 ± 33.7
HDFS 1-182......	2.8 ± 2.0	0.3 ± 1.0	3.5 ± 0.7	7.0 ± 1.2	85.2 ± 11.5	211.3 ± 22.0	279.8 ± 18.5	261.7 ± 18.1
HDFS 1-186......	89.2 ± 1.9	234.9 ± 0.9	577.6 ± 0.6	963.1 ± 1.2	1605.1 ± 11.5	1933.2 ± 22.0	2194.5 ± 18.5	2992.2 ± 37.2
HDFS 1-194......	4.5 ± 2.0	12.6 ± 1.0	35.3 ± 0.6	48.1 ± 1.2	109.0 ± 11.5	156.7 ± 22.0	289.2 ± 18.5	295.6 ± 27.3
HDFS 1-187......	32.5 ± 1.9	71.2 ± 0.9	136.3 ± 0.6	317.6 ± 1.2	858.0 ± 11.5	1201.0 ± 22.0	1794.9 ± 18.5	2208.2 ± 32.7
HDFS 1-188......	19.8 ± 1.6	31.8 ± 0.8	66.5 ± 0.5	130.6 ± 1.0	189.0 ± 9.9	245.9 ± 19.1	248.3 ± 16.0	237.8 ± 17.0
HDFS 1-207......	25.6 ± 2.0	116.9 ± 1.0	478.8 ± 0.6	1439.3 ± 1.2	3169.8 ± 11.5	4177.3 ± 22.0	4909.9 ± 18.6	5594.4 ± 34.5
HDFS 1-232......	94.7 ± 2.1	149.3 ± 1.0	308.3 ± 0.7	498.4 ± 1.2	630.5 ± 11.5	728.9 ± 22.0	715.6 ± 18.5	735.2 ± 24.3
HDFS 1-236......	42.8 ± 2.4	59.9 ± 1.2	112.0 ± 0.7	179.1 ± 1.4	244.1 ± 11.5	244.9 ± 22.0	281.0 ± 18.5	301.7 ± 33.7
HDFS 1-237......	40.2 ± 2.4	73.1 ± 1.1	153.6 ± 0.7	298.7 ± 1.4	418.8 ± 11.5	583.9 ± 22.1	576.1 ± 18.6	721.1 ± 29.2
HDFS 1-276......	13.1 ± 2.3	38.3 ± 1.1	46.9 ± 0.7	78.6 ± 1.5	189.8 ± 11.5	247.7 ± 22.0	287.5 ± 18.5	292.4 ± 24.9
HDFS 1-283......	12.2 ± 2.3	30.5 ± 1.1	43.1 ± 0.7	70.9 ± 1.4	158.1 ± 11.5	256.2 ± 22.0	232.2 ± 18.5	219.4 ± 19.3
HDFS 1-286......	17.6 ± 3.3	51.4 ± 1.6	57.1 ± 0.9	84.4 ± 1.9	152.3 ± 11.5	213.0 ± 22.0	218.4 ± 18.5	206.2 ± 17.7
HDFS 1-287......	64.9 ± 2.5	94.3 ± 1.3	132.8 ± 0.8	271.7 ± 1.7	491.0 ± 10.8	492.8 ± 20.8	592.0 ± 17.5	622.7 ± 23.8
HDFS 1-302......	12.9 ± 2.4	34.0 ± 1.1	118.3 ± 0.7	307.7 ± 1.6	611.2 ± 11.5	797.7 ± 22.0	1006.4 ± 18.5	967.5 ± 22.5
HDFS 1-289......	233.6 ± 2.6	498.0 ± 1.3	989.8 ± 0.8	1917.0 ± 1.8	3402.5 ± 11.5	4810.0 ± 22.0	5790.5 ± 18.5	7104.0 ± 37.7
HDFS 1-291......	-0.6 ± 2.2	5.4 ± 1.0	14.2 ± 0.7	72.1 ± 1.3	358.2 ± 11.5	547.6 ± 22.1	733.7 ± 18.6	700.0 ± 19.6
HDFS 1-299......	77.2 ± 2.1	156.7 ± 1.0	346.1 ± 0.7	688.6 ± 1.2	1139.6 ± 11.5	1435.2 ± 22.0	1619.5 ± 18.5	2788.3 ± 44.4
HDFS 1-306......	2.0 ± 2.1	19.8 ± 1.0	24.6 ± 0.7	40.3 ± 1.3	103.1 ± 11.5	95.0 ± 22.0	181.2 ± 18.5	177.3 ± 18.0
HDFS 1-313......	39.5 ± 2.1	59.8 ± 1.0	117.5 ± 0.7	201.4 ± 1.2	249.6 ± 11.5	328.6 ± 22.0	333.4 ± 18.5	351.2 ± 25.6
HDFS 1-317......	-3.4 ± 2.1	7.8 ± 1.1	11.4 ± 0.7	31.3 ± 1.4	23.4 ± 11.3	81.7 ± 21.7	109.4 ± 18.3	159.1 ± 26.4
HDFS 1-318......	13.2 ± 2.1	141.6 ± 1.0	546.9 ± 0.7	1140.3 ± 1.2	2001.0 ± 11.5	2422.8 ± 22.0	2745.0 ± 18.6	3336.3 ± 34.5
HDFS 1-335......	5.6 ± 2.3	42.6 ± 1.1	58.7 ± 0.7	71.1 ± 1.4	91.6 ± 11.5	213.1 ± 22.1	233.1 ± 18.6	250.0 ± 24.8
HDFS 1-326......	56.3 ± 2.1	69.0 ± 1.0	111.8 ± 0.7	193.5 ± 1.2	175.9 ± 11.5	277.8 ± 22.0	191.7 ± 18.5	172.5 ± 17.4
HDFS 1-332......	61.1 ± 2.0	170.2 ± 1.0	415.1 ± 0.7	725.6 ± 1.2	1140.3 ± 11.5	1462.2 ± 22.0	1681.7 ± 18.5	1727.9 ± 26.5
HDFS 1-334......	10.1 ± 2.1	38.1 ± 1.0	86.6 ± 0.7	231.1 ± 1.2	873.6 ± 11.5	1478.9 ± 22.0	2203.7 ± 18.5	2577.4 ± 33.0
HDFS 1-340......	39.9 ± 3.8	67.8 ± 1.4	131.6 ± 0.9	228.2 ± 1.8	315.4 ± 11.5	350.1 ± 22.0	384.4 ± 18.6	433.6 ± 24.5
HDFS 1-342......	50.0 ± 1.9	69.0 ± 1.0	101.2 ± 0.6	193.5 ± 1.2	254.3 ± 11.5	259.2 ± 22.0	307.0 ± 18.6	297.6 ± 19.7
HDFS 1-346......	28.6 ± 2.1	47.1 ± 1.0	94.0 ± 0.7	143.0 ± 1.2	161.6 ± 11.5	187.3 ± 22.0	214.6 ± 18.5	280.7 ± 32.4

TABLE 1—*Continued*

ID	F300W[a]	F450W[a]	F606W[a]	F814W[a]	J_s[a]	H[a]	K_s[a]	K_s^{tot}[b]
HDFS 1-347......	5.2 ± 2.1	19.7 ± 1.0	41.1 ± 0.7	52.9 ± 1.2	60.7 ± 11.5	162.8 ± 22.0	179.3 ± 18.5	214.5 ± 27.1
HDFS 1-345......	41.1 ± 1.9	207.3 ± 1.0	821.0 ± 0.7	2147.5 ± 1.2	5113.4 ± 11.5	8029.0 ± 22.1	10027.0 ± 18.6	12210.0 ± 38.4
HDFS 1-350......	−0.2 ± 2.0	3.9 ± 1.0	9.1 ± 0.7	19.0 ± 1.2	90.0 ± 14.7	169.1 ± 27.8	373.7 ± 23.7	393.7 ± 28.1
HDFS 1-355......	3.9 ± 2.1	4.6 ± 1.0	5.7 ± 0.7	12.2 ± 1.2	12.2 ± 11.5	106.0 ± 22.0	169.3 ± 18.5	165.1 ± 17.4
HDFS 1-354......	3.4 ± 1.6	9.6 ± 0.8	12.0 ± 0.5	22.1 ± 1.0	77.4 ± 9.4	203.5 ± 18.0	155.8 ± 15.2	151.6 ± 21.3
HDFS 1-364......	81.1 ± 1.9	117.4 ± 0.9	164.0 ± 0.6	274.9 ± 1.2	388.1 ± 11.4	452.9 ± 21.9	515.8 ± 18.5	606.4 ± 35.9
HDFS 1-363......	50.1 ± 2.0	115.3 ± 1.0	158.0 ± 0.7	268.8 ± 1.2	580.5 ± 11.5	705.6 ± 22.0	791.4 ± 18.5	781.4 ± 21.8
HDFS 1-360......	27.1 ± 1.9	86.4 ± 1.0	114.0 ± 0.6	198.9 ± 1.2	561.7 ± 11.4	776.6 ± 21.9	817.3 ± 18.4	1071.2 ± 34.3
HDFS 1-368......	36.1 ± 1.9	60.0 ± 0.9	67.7 ± 0.6	123.8 ± 1.2	195.2 ± 11.5	190.1 ± 22.0	232.7 ± 18.5	250.7 ± 23.4
HDFS 1-372......	32.4 ± 1.8	75.8 ± 0.9	172.0 ± 0.6	336.5 ± 1.1	483.2 ± 10.4	593.5 ± 20.0	700.0 ± 16.9	754.1 ± 23.2
HDFS 1-373......	34.1 ± 1.8	70.7 ± 0.9	112.0 ± 0.6	202.1 ± 1.1	388.1 ± 10.3	445.5 ± 19.7	595.3 ± 16.6	607.9 ± 21.9
HDFS 1-378......	9.2 ± 2.0	72.6 ± 1.0	98.4 ± 0.7	130.4 ± 1.2	311.1 ± 11.5	422.2 ± 22.1	499.1 ± 18.6	648.2 ± 40.3
HDFS 1-379......	38.0 ± 2.1	67.8 ± 1.0	124.7 ± 0.7	345.9 ± 1.2	1373.1 ± 11.5	2079.8 ± 22.0	2726.2 ± 18.5	2881.6 ± 28.2
HDFS 1-377......	2.1 ± 2.1	15.7 ± 1.0	34.2 ± 0.7	130.2 ± 1.3	700.4 ± 11.5	1090.0 ± 22.0	1551.8 ± 18.5	1590.3 ± 24.9
HDFS 1-380......	−3.1 ± 1.9	8.8 ± 0.9	23.7 ± 0.6	101.9 ± 1.2	291.4 ± 11.5	408.5 ± 22.0	518.0 ± 18.6	478.4 ± 20.0
HDFS 1-381......	18.4 ± 1.9	37.3 ± 0.9	45.5 ± 0.6	83.8 ± 1.2	121.8 ± 11.5	184.8 ± 22.0	219.2 ± 18.5	213.9 ± 21.5
HDFS 1-382......	−2.7 ± 1.9	24.9 ± 0.9	31.2 ± 0.6	45.8 ± 1.2	70.6 ± 11.4	121.7 ± 21.9	191.8 ± 18.4	206.7 ± 24.9
HDFS 1-386......	13.7 ± 1.9	102.0 ± 0.9	139.6 ± 0.6	191.4 ± 1.2	462.9 ± 11.5	575.7 ± 22.0	620.5 ± 18.5	665.6 ± 26.6
HDFS 1-383......	65.3 ± 1.9	119.3 ± 0.9	266.5 ± 0.6	412.6 ± 1.2	543.2 ± 11.5	642.0 ± 22.0	656.8 ± 18.5	1037.5 ± 44.3
HDFS 1-424......	0.0 ± 1.9	2.3 ± 0.9	7.6 ± 0.6	35.7 ± 1.2	31.3 ± 11.5	48.8 ± 22.0	152.9 ± 18.5	177.3 ± 35.0
HDFS 1-393......	5.0 ± 1.9	33.0 ± 0.9	47.7 ± 0.6	75.6 ± 1.2	284.3 ± 11.5	352.9 ± 22.0	544.6 ± 18.5	664.9 ± 30.4
HDFS 1-394......	4.5 ± 1.9	25.6 ± 1.0	63.6 ± 0.6	109.9 ± 1.2	161.7 ± 13.0	198.9 ± 25.0	188.0 ± 21.1	308.1 ± 41.0
HDFS 1-395......	73.1 ± 2.1	291.9 ± 1.0	603.1 ± 0.7	930.9 ± 1.2	1321.3 ± 11.5	1516.6 ± 22.1	1554.7 ± 18.6	1947.7 ± 33.0
HDFS 1-397......	14.4 ± 2.1	23.4 ± 1.0	38.7 ± 0.7	94.8 ± 1.2	323.4 ± 11.5	526.9 ± 22.1	778.5 ± 18.6	952.8 ± 34.7
HDFS 1-399......	57.9 ± 2.0	89.7 ± 1.0	180.2 ± 0.7	315.6 ± 1.2	410.7 ± 11.5	532.8 ± 22.0	568.3 ± 18.5	546.5 ± 23.4
HDFS 1-404......	27.3 ± 2.9	43.4 ± 1.2	70.1 ± 0.8	112.3 ± 1.5	151.1 ± 11.5	153.3 ± 22.0	186.8 ± 18.6	261.2 ± 33.6
HDFS 1-405......	5.1 ± 1.9	3.3 ± 0.9	9.2 ± 0.6	47.5 ± 1.2	258.1 ± 11.5	341.2 ± 22.0	541.7 ± 18.5	565.7 ± 25.5
HDFS 1-398......	1.1 ± 1.9	1.8 ± 0.9	5.0 ± 0.6	24.1 ± 1.1	84.8 ± 10.7	141.2 ± 20.4	231.5 ± 17.2	335.1 ± 31.0
HDFS 1-406......	118.8 ± 2.1	343.0 ± 1.0	1174.0 ± 0.7	3242.7 ± 1.2	7359.3 ± 11.5	10974.2 ± 22.0	13863.9 ± 18.5	21541.4 ± 49.5
HDFS 1-411......	11.1 ± 2.2	6.6 ± 1.1	16.2 ± 0.7	41.3 ± 1.3	134.5 ± 11.5	235.4 ± 22.0	361.3 ± 18.5	370.4 ± 28.9
HDFS 1-427......	10.5 ± 1.9	16.1 ± 0.9	22.5 ± 0.6	42.8 ± 1.2	148.6 ± 11.5	186.9 ± 22.0	264.1 ± 18.5	261.3 ± 20.2
HDFS 1-414......	26.6 ± 1.9	89.1 ± 1.0	236.7 ± 0.7	526.1 ± 1.2	1248.8 ± 11.5	2030.9 ± 22.1	2714.7 ± 18.6	2770.6 ± 26.2
HDFS 1-410......	85.3 ± 2.0	144.6 ± 1.0	285.7 ± 0.7	491.4 ± 1.2	671.5 ± 11.5	782.2 ± 22.0	882.8 ± 18.5	1481.1 ± 41.1
HDFS 1-415......	61.0 ± 1.9	116.1 ± 0.9	252.7 ± 0.7	415.9 ± 1.2	552.8 ± 11.5	673.8 ± 22.0	637.9 ± 18.5	839.5 ± 33.0
HDFS 1-421......	121.1 ± 1.9	428.1 ± 0.9	1243.9 ± 0.6	2490.1 ± 1.2	4647.2 ± 11.6	6378.8 ± 22.3	7614.6 ± 18.7	9886.4 ± 40.3
HDFS 1-426......	13.0 ± 2.1	15.4 ± 1.0	33.9 ± 0.7	85.1 ± 1.2	259.9 ± 11.5	465.1 ± 22.1	659.7 ± 18.6	639.4 ± 21.6
HDFS 1-434......	15.6 ± 2.0	15.9 ± 1.0	41.1 ± 0.7	84.0 ± 1.2	119.2 ± 11.5	170.4 ± 22.0	230.1 ± 18.5	250.1 ± 20.6
HDFS 1-435......	1.6 ± 2.0	13.8 ± 1.0	37.6 ± 0.7	89.5 ± 1.2	139.1 ± 11.5	193.4 ± 22.0	227.9 ± 18.6	244.0 ± 31.9
HDFS 1-437......	49.1 ± 2.0	69.2 ± 1.0	81.6 ± 0.	127.7 ± 1.2	201.1 ± 11.5	226.5 ± 22.1	285.0 ± 18.6	288.0 ± 23.0
HDFS 1-439......	93.5 ± 1.9	140.1 ± 0.9	212.6 ± 0.6	382.9 ± 1.2	496.9 ± 11.5	610.1 ± 22.0	637.5 ± 18.5	851.0 ± 36.3
HDFS 1-440......	6.2 ± 1.9	0.1 ± 0.9	6.7 ± 0.6	33.9 ± 1.2	284.0 ± 11.5	569.8 ± 22.0	781.8 ± 18.5	785.1 ± 24.6
HDFS 1-448......	31.5 ± 2.3	62.4 ± 1.1	71.2 ± 0.8	100.2 ± 1.4	198.3 ± 11.8	264.2 ± 22.5	258.6 ± 19.0	314.4 ± 28.7
HDFS 1-450......	20.0 ± 1.7	27.1 ± 0.9	65.5 ± 0.6	102.8 ± 1.1	88.8 ± 10.7	78.6 ± 20.6	125.8 ± 17.3	167.4 ± 29.7
HDFS 1-463......	−0.5 ± 1.9	15.4 ± 0.9	20.5 ± 0.6	26.9 ± 1.2	69.1 ± 11.5	87.9 ± 22.0	216.9 ± 18.6	234.5 ± 21.0
HDFS 1-484......	6.0 ± 2.1	64.3 ± 1.0	353.4 ± 0.7	1138.1 ± 1.3	2428.7 ± 11.5	3465.8 ± 22.0	4114.4 ± 18.5	4158.8 ± 26.3
HDFS 1-472......	12.2 ± 2.1	36.7 ± 1.0	74.9 ± 0.7	168.4 ± 1.2	253.0 ± 11.5	339.9 ± 22.0	350.5 ± 18.5	367.6 ± 21.9
HDFS 1-476......	27.0 ± 1.8	49.8 ± 0.9	59.1 ± 0.6	97.2 ± 1.2	186.9 ± 11.5	193.6 ± 22.0	210.5 ± 18.5	208.1 ± 27.9
HDFS 1-480......	−2.5 ± 2.1	2.3 ± 1.0	0.3 ± 0.7	1.7 ± 1.3	16.8 ± 11.5	70.4 ± 22.0	174.6 ± 18.5	171.6 ± 20.0
HDFS 1-479......	5.7 ± 1.9	12.1 ± 0.9	26.3 ± 0.7	47.0 ± 1.2	156.2 ± 11.5	217.7 ± 22.0	378.9 ± 18.5	388.5 ± 21.4
HDFS 1-483......	4.4 ± 1.8	34.1 ± 0.9	43.9 ± 0.6	58.8 ± 1.2	155.8 ± 11.5	185.6 ± 22.1	266.2 ± 18.6	328.1 ± 28.8
HDFS 1-487......	3.0 ± 2.1	1.8 ± 1.0	4.4 ± 0.7	16.4 ± 1.2	55.2 ± 11.5	187.5 ± 22.0	213.5 ± 18.5	196.5 ± 17.8
HDFS 1-488......	42.3 ± 2.1	92.3 ± 1.0	235.8 ± 0.7	493.2 ± 1.2	873.6 ± 11.5	1245.4 ± 22.0	1533.3 ± 18.5	1947.3 ± 32.3
HDFS 1-492......	19.7 ± 2.1	31.9 ± 1.0	44.5 ± 0.7	57.7 ± 1.3	105.6 ± 11.5	100.6 ± 22.0	147.5 ± 18.5	164.7 ± 24.0
HDFS 1-489......	46.1 ± 2.	96.0 ± 1.0	236.3 ± 0.7	513.2 ± 1.3	934.6 ± 11.5	1322.8 ± 22.0	1568.4 ± 18.6	1647.6 ± 26.6
HDFS 1-478......	47.4 ± 2.2	77.4 ± 1.0	97.1 ± 0.7	176.7 ± 1.3	553.1 ± 11.5	682.6 ± 22.0	907.6 ± 18.5	1157.7 ± 37.3
HDFS 1-505......	2.3 ± 1.9	35.3 ± 1.0	50.0 ± 0.6	93.3 ± 1.2	265.1 ± 11.5	438.4 ± 22.0	423.6 ± 18.5	425.5 ± 20.3
HDFS 1-511......	28.5 ± 2.3	63.3 ± 1.1	97.3 ± 0.7	190.9 ± 1.3	451.0 ± 11.5	669.7 ± 22.1	889.9 ± 18.6	962.4 ± 26.5
HDFS 1-516......	48.9 ± 3.4	68.8 ± 1.4	126.7 ± 0.9	188.2 ± 1.7	205.6 ± 11.5	268.6 ± 22.0	229.7 ± 18.5	381.8 ± 37.0
HDFS 1-542......	3.7 ± 2.4	28.3 ± 1.1	81.2 ± 0.8	139.0 ± 1.3	216.4 ± 11.5	195.7 ± 22.0	291.6 ± 18.5	293.5 ± 23.1
HDFS 1-521......	80.4 ± 2.8	177.6 ± 1.3	427.4 ± 0.9	875.4 ± 1.5	1620.2 ± 11.6	2313.2 ± 22.3	2721.3 ± 18.8	3263.4 ± 35.
HDFS 1-522......	13.2 ± 2.0	29.7 ± 1.0	58.3 ± 0.7	109.2 ± 1.2	145.8 ± 15.6	111.6 ± 29.3	232.5 ± 25.1	222.4 ± 26.0
HDFS 1-530......	26.2 ± 3.5	52.3 ± 1.6	73.6 ± 1.0	158.6 ± 1.8	357.5 ± 11.5	395.9 ± 22.0	520.6 ± 18.5	531.7 ± 24.6
HDFS 1-536......	25.1 ± 1.9	43.8 ± 1.0	66.0 ± 0.7	144.9 ± 1.2	203.9 ± 11.5	257.9 ± 22.0	258.4 ± 18.5	294.0 ± 32.1
HDFS 1-527......	31.0 ± 2.0	59.3 ± 1.0	104.5 ± 0.7	299.5 ± 1.2	1278.7 ± 11.5	2125.7 ± 22.0	2883.0 ± 18.6	3437.7 ± 35.1
HDFS 1-538......	97.8 ± 2.4	162.6 ± 1.1	294.2 ± 0.8	504.3 ± 1.4	706.7 ± 11.5	962.7 ± 22.1	1025.3 ± 18.6	1059.7 ± 25.0
HDFS 1-548......	12.9 ± 2.3	8.5 ± 1.1	41.6 ± 0.8	174.2 ± 1.3	508.4 ± 11.5	787.7 ± 22.1	835.5 ± 18.6	922.8 ± 30.2
HDFS 1-555......	−5.9 ± 3.0	8.5 ± 1.5	22.7 ± 1.1	95.6 ± 1.6	427.0 ± 12.7	743.0 ± 24.5	1202.9 ± 20.5	1204.0 ± 26.4

NOTE.—All fluxes are in units of 10^{-31} ergs s^{-1} Hz^{-1} cm^{-2}.
[a] Fluxes measured over a 2″.0 diameter aperture.
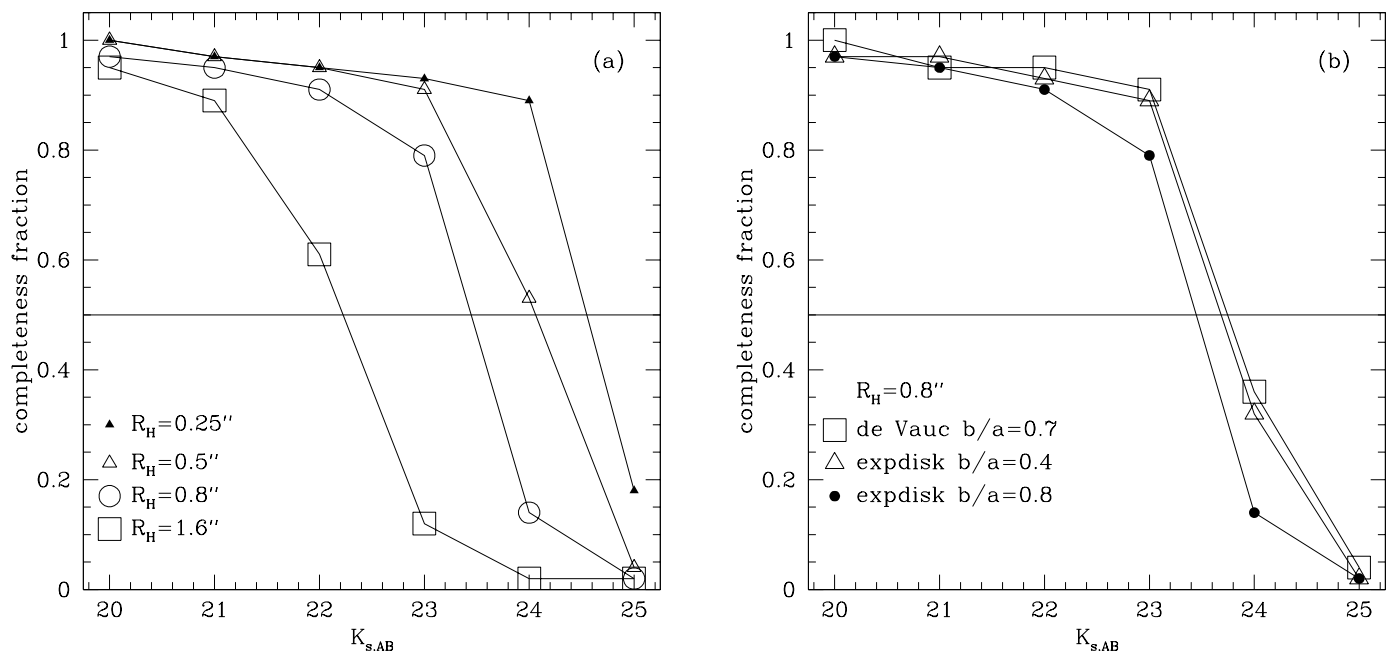[b] The "AUTO" flux from SExtractor with a minimum 2″.0 diameter aperture.

FIG. 2.—Estimates of the K_s-band completeness limit. (a) Completeness against $K_{s,AB}$ magnitude for galaxies with an exponential profile and an axis ratio of $b/a = 0.8$. Different points represent different galaxy half-light radii, R_H. Note how the completeness dependents greatly on the object size. (b) Completeness vs. $K_{s,AB}$ magnitude at the typical faint object radius of $R_H = 0\rlap{.}''8$ for three different profile shapes. The completeness is relatively insensitive to the exact profile shape. In both plots, the horizontal line shows the 50% completeness limit.

are least complete, the exponential disk with $b/a = 0.8$ (see Fig. 2b). Using this curve (see Fig. 2a), we established a 50% completeness limit at $K_{s,AB} = 23.5$ and note that we are 90% complete for $K_{s,AB} < 22.0$. For this flux limit, our conclusions are insensitive to completeness corrections, and so we make no such corrections.

3. PHOTOMETRIC REDSHIFTS

3.1. *Template Choice*

The next step in the analysis is to convert the flux measurements of objects in the seven bands into an estimate of their redshift. We estimate the redshifts of our galaxies by modeling their rest-frame colors by a combination of empirical spectral templates. We used Hubble type templates E, Sbc, Scd, and Im from Coleman, Wu, & Weedman (1980, hereafter CWW80) and the two starburst templates with a low derived reddening, designated SB1 and SB2, from Kinney et al. (1996). For the two starburst templates, the color excess $E(B-V)$ with respect to the expected colors of an unreddened galaxy is ≤ 0.10 and $0.11 \leq E(B-V) \leq 0.21$, respectively. These templates are needed because many galaxies even in the nearby universe have colors bluer than the bluest CWW80 templates, and the inclusion of SB1 and SB2 significantly improves the photometric redshift estimate (see also Sawicki, Lin, & Yee 1997; Benítez 2000).

To extend the CWW80 and starburst templates from their published short-wavelength limits (1400 and 1232 Å, respectively) to below the LB, we extrapolated blueward a power-law fit to the 1400–1800 and 1240–1740 Å wavelength ranges, respectively. To account for intervening absorption from neutral cosmic hydrogen, we applied to all our template spectra the redshift-dependent cosmic mean opacity taken from Madau (1995). We accounted for the internal hydrogen absorption of the galaxy by setting the

flux blueward of 912 Å to zero. To extend the templates to the IR, we used the stellar population synthesis code of Bruzual & Charlot (2001). We constructed NIR SED extensions for each template by using the stellar population ages, star formation timescales, and initial mass functions for each template Hubble type from Pozzetti, Bruzual, & Zamorani (1996; see Table 2). We verified that these SEDs matched the optical colors of our templates.

In addition to the "natural" reddening already included in the templates, additional reddening may be present. We will examine the effect of reddening on the determination of z_{phot} in Labbé et al. (2001).

3.2. *Template-based Estimates of the Redshift*

We cannot assume a priori that distant galaxies have SEDs identical to any one of our empirical SEDs. In fact, even within a single galaxy there may be spatial variations in the stellar populations and SFRs. Our goal is to fit the observed flux points as well as possible with minimal assumptions about the galaxy's SFH. Therefore, we attempt to model the observed SED by a *linear combination* of redshifted templates. We estimate the likelihood that a galaxy

TABLE 2
NIR TEMPLATE EXTENSION PARAMETERS

Template	Age (Gyr)	IMF	SFR
E/S0......	12.7	Scalo	$\tau = 1$ Gyr
Sbc.......	12.7	Scalo	$\tau = 8$ Gyr
Scd.......	12.7	Salpeter	Constant
Irr........	0.1	Salpeter	Constant
SB1	0.1	Salpeter	Constant
SB2	0.1	Salpeter	Constant

lies at a given redshift by calculating

$$\chi^2(z) = \sum_{i=1}^{N_{\text{filter}}} \left[\frac{F_i^{\text{data}} - F_i^{\text{model}}}{\sigma_i^{\text{data}}} \right]^2 , \qquad (2)$$

where F_i^{data} is the measured flux value in units of f_λ in the ith color bandpass, σ_i^{data} is its associated $1\,\sigma$ uncertainty, and

$$F_i^{\text{model}} = \sum_{j=1}^{N_{\text{template}}} C^j F_i^j(z) , \qquad (3)$$

where the $F_i^j(z)$ is the flux of the jth template, redshifted to z, adjusted for intervening cosmic hydrogen absorption, and integrated over the transmission curve of the ith filter. For every redshift, we determine the nonnegative coefficients C^j, which minimize χ^2 and the most likely photometric redshift, z_{phot}, which is the minimum of $\chi^2(z)$. To determine how our photometric errors propagate to errors in z_{phot}, we performed a Monte Carlo simulation, where for each object we create 200 synthetic photometry measurements distributed like a Gaussian around the observed flux, with a width $\sigma = \sigma_i^{\text{data}}$. For each object's Monte Carlo set of fluxes, we determined individually the values of z_{phot} and calculated its 68% confidence limits, δz_{MC}, from the resulting distribution. We added a systematic error component in § 3.3.3 to obtain the final error estimate δz_{phot}. From this point on, all values of z_{phot} will refer to those calculated directly from the catalog data. The values of z_{phot} and δz_{phot} are given in Table 3.

3.3. Comparison With Spectroscopic Redshifts

3.3.1. Hubble Deep Field North

We gauged the precision and accuracy of our photometric redshift technique against spectroscopic redshifts using the data set provided by Cohen et al. (2000) on the HDF-N. This field has optical data from *HST* (Williams et al. 1996) and *JHK* data from the IRIM camera on the Kitt Peak 4 m telescope taken by Dickinson (2001a) in April of 1996. Using the photometry of FLY99, we derive the photometric redshifts of all the F814W-selected objects in the HDF-N using our code. There are a total of 150 objects common between the Cohen et al. spectroscopic sample and the FLY99 photometric sample. The comparison between our photometric redshifts, z_{phot}, and the spectroscopic redshifts, z_{spec}, for this sample is shown in Figure 3. The redshift error bars here are those calculated from the Monte Carlo simulation, δz_{MC} (see § 3.2). We choose for our measure of photometric redshift accuracy

$$\Delta z = |z_{\text{spec}} - z_{\text{phot}}| . \qquad (4)$$

Our mean value is $\Delta z \approx 0.14$ for $z \leq 1.5$ and $\Delta z \approx 0.44$ for $z > 1.5$. We also note that the value $\Delta z/(1+z)$ is nearly constant with redshift with $\Delta z/(1+z) \approx 0.09$ for the whole sample. This was first noted by FLY99 and likely stems from the effect that the filter spacing is roughly constant in $\ln \lambda$, and the redshift determination is equivalent to finding a constant shift $\ln(1+z)$ for the spectrum if it is expressed as a function of $\ln \lambda$.

We note that there are a few objects ($\lesssim 3\%$) for which z_{phot} and z_{spec} are greatly different, in part because there appear to be galaxies whose SEDs cannot be represented by our template set. In addition, Fernández-Soto et al. (2001; hereafter FS01) suggested that five of the published spectroscopic redshifts may be in error. One of these objects (FS01 identification number HDF 36441_1410) has a $z_{\text{spec}} = 2.267$
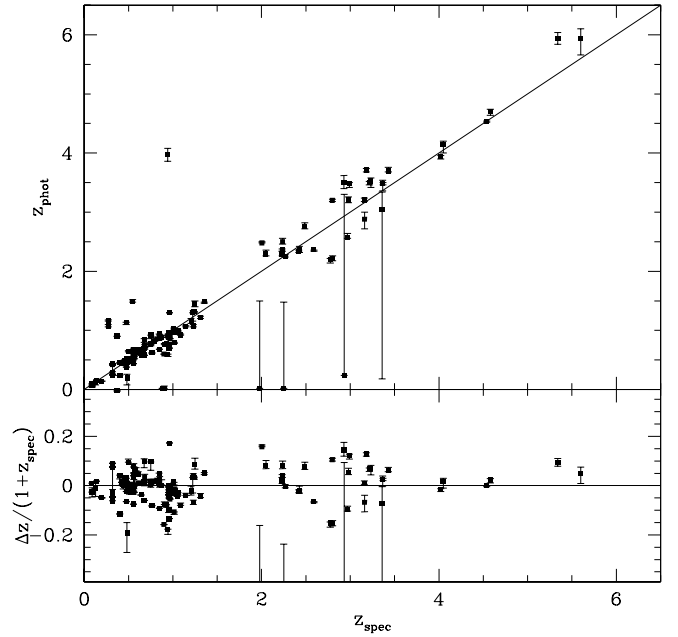

FIG. 3.—Comparison of z_{phot} to z_{spec} for objects in the WFPC2 field of the HDF-N. The error bars are derived from our Monte Carlo simulations. The top panel shows a direct comparison between z_{phot} and z_{spec}. The diagonal line corresponds to a one-to-one relation to guide the eye. The bottom panel shows how z_{spec} relates to the difference between z_{phot} and z_{spec} normalized by $1 + z_{\text{spec}}$. The agreement is excellent for $z_{\text{spec}} < 6.0$, with only $\lesssim 3\%$ of the sample having $|z_{\text{spec}} - z_{\text{phot}}| > 1.0$ and with $\Delta z/(1+z) = 0.07$. The Monte Carlo errors serve as a good indication of possible catastrophic failures of the z_{phot} determination.

and is found by FS01 to have $z_{\text{phot}} = 0.01$. We, however, find $z_{\text{phot}} = 2.26$, in excellent agreement with the spectroscopic redshift. Eliminating HDF 36441_1410 causes almost no change in Δz or $\Delta z/(1+z)$ for $z > 1.5$. Four objects remain[11] for which we found that our z_{phot} values do not agree well with the published z_{spec} values. These objects all lie at $z_{\text{spec}} < 1$. When eliminating these four objects, we found that Δz decreased to ≈ 0.10 for $z \leq 1.5$. With these four objects removed the mean $\Delta z/(1+z)$ for the redshift range $z < 6$ is 0.07. There are three objects with $z_{\text{spec}} = 2.931, 2.250,$ and 1.980 that are not flagged by FS01 as having incorrect spectroscopic redshifts (FS01 identifications HDF 36478_1255, 36446_1227, and 36498_1415) for which we find $z_{\text{phot}} = 0.024, 0.02,$ and 0.02 and for which FS01 find $z_{\text{phot}} = 0.26, 2.47,$ and 1.64. In all three of these cases, δz_{MC} is large and so, in general, may provide a good indicator of discrepant z_{phot} values.

To test the importance of the NIR data in determining the correct redshift, we compare the accuracy of z_{phot} in the HDF-N as derived with and without NIR data. The NIR data is excluded from the fit by setting the error term to infinity in the χ^2 sum. For $z_{\text{spec}} \leq 1.5$, the advantage of the NIR data is obvious, with the mean value of Δz increasing from 0.10 to 0.21 when the NIR data is not included. For two galaxies (FS01 identifications HDF 36498_1415 and 36446_1227) with $z_{\text{spec}} = 1.98$ and $z_{\text{spec}} = 2.25$, however, excluding the NIR data causes z_{phot} to change from 0.20 to 2.24 and from 0.20 to 2.20, respectively. The original esti-

---

[11] Fernández-Soto et al. (2001) identification numbers HDF 36396_1230, 36494_1317, 36561_1330, and 36569_1302.

TABLE 3

ID	R.A. (22^h)	Decl. ($-60°$)	z_{phot}	L_U^{rest} (10^{10} $L_\odot$)	L_B^{rest} (10^{10} $L_\odot$)	L_V^{rest} (10^{10} $L_\odot$)
HDFS 1-30	32 52.26	31 52.7	$1.36_{0.17}^{0.17}$	$3.74_{1.40}^{1.43}$	$2.53_{0.94}^{1.00}$	$2.36_{0.86}^{0.96}$
HDFS 1-33	32 52.69	31 53.0	$0.92_{0.14}^{0.13}$	$0.59_{0.25}^{0.27}$	$0.34_{0.13}^{0.18}$	$0.29_{0.11}^{0.17}$
HDFS 1-31	32 52.04	31 54.1	$0.62_{0.13}^{0.15\,a}$	$0.12_{0.06}^{0.09}$	$0.07_{0.04}^{0.05}$	$0.07_{0.03}^{0.05}$
HDFS 1-36	32 48.84	31 54.1	$3.32_{0.31}^{0.30}$	$16.53_{0.98}^{4.64}$	$9.21_{0.38}^{2.50}$	$8.13_{0.49}^{3.08}$
HDFS 1-37	32 53.38	31 54.5	$3.00_{0.37}^{0.63\,a}$	$5.06_{1.92}^{4.47}$	$5.25_{1.99}^{4.64}$	$6.62_{2.50}^{5.88}$
HDFS 1-45^b	32 56.18	31 56.6	$5.34_{0.45}^{0.44}$	$59.89_{14.96}^{11.84}$	$32.92_{6.75}^{0.11}$	$27.59_{6.67}^{0.08}$
HDFS 1-50	32 49.45	31 58.1	$1.22_{0.16}^{0.28}$	$0.28_{0.12}^{0.40}$	$0.32_{0.13}^{0.33}$	$0.43_{0.17}^{0.35}$
HDFS 1-52	32 54.06	31 58.1	$1.22_{0.18}^{0.16\,a}$	$1.57_{0.51}^{0.49}$	$0.89_{0.33}^{0.24}$	$0.69_{0.25}^{0.19}$
HDFS 1-54	32 52.98	31 58.4	$1.08_{0.28}^{0.15}$	$0.53_{0.29}^{0.25}$	$0.32_{0.20}^{0.15}$	$0.27_{0.16}^{0.15}$
HDFS 1-62	32 50.35	32 01.0	$1.00_{0.17}^{0.14}$	$0.63_{0.26}^{0.29}$	$0.40_{0.18}^{0.21}$	$0.35_{0.16}^{0.19}$
HDFS 1-58	32 53.38	32 01.3	$1.02_{0.14}^{0.14}$	$0.52_{0.26}^{0.39}$	$0.60_{0.27}^{0.30}$	$0.79_{0.33}^{0.31}$
HDFS 1-63	32 50.28	32 03.5	$0.44_{0.10}^{0.10}$	$0.40_{0.21}^{0.26}$	$0.26_{0.13}^{0.16}$	$0.25_{0.12}^{0.13}$
HDFS 1-69	32 48.80	32 03.5	$0.84_{0.13}^{0.24}$	$0.43_{0.18}^{0.48}$	$0.25_{0.10}^{0.32}$	$0.24_{0.08}^{0.29}$
HDFS 1-74	32 53.70	32 06.0	$0.96_{0.14}^{0.14}$	$1.01_{0.48}^{0.85}$	$0.90_{0.40}^{0.58}$	$1.05_{0.42}^{0.50}$
HDFS 1-79	32 49.06	32 06.0	$2.22_{0.24}^{0.23\,a}$	$10.13_{2.31}^{2.32}$	$5.54_{1.20}^{0.99}$	$4.26_{0.94}^{0.81}$
HDFS 1-80	32 51.86	32 06.0	$3.24_{0.30}^{0.30}$	$8.00_{0.67}^{1.48}$	$4.07_{0.23}^{0.28}$	$3.21_{0.14}^{0.26}$
HDFS 1-83	32 52.73	32 07.1	$0.46_{0.10}^{0.10}$	$0.62_{0.30}^{0.40}$	$0.39_{0.19}^{0.20}$	$0.35_{0.15}^{0.17}$
HDFS 1-86	32 46.68	32 07.1	$0.16_{0.08}^{0.08}$	$0.02_{0.01}^{0.03}$	$0.01_{0.01}^{0.02}$	$0.01_{0.01}^{0.02}$
HDFS 1-87	32 54.82	32 08.2	$1.60_{0.21}^{1.93\,a}$	$0.87_{0.30}^{6.98}$	$0.63_{0.23}^{5.03}$	$0.62_{0.23}^{4.87}$
HDFS 1-92	32 56.26	32 09.6	$1.38_{0.18}^{0.18}$	$0.99_{0.40}^{0.40}$	$0.68_{0.25}^{0.28}$	$0.63_{0.21}^{0.27}$
HDFS 1-98	32 55.72	32 11.4	$0.56_{0.11}^{0.11}$	$0.45_{0.23}^{0.46}$	$0.58_{0.29}^{0.40}$	$0.80_{0.40}^{0.46}$
HDFS 1-105......	32 49.24	32 11.8	$2.14_{0.27}^{0.22}$	$1.70_{0.73}^{0.67}$	$1.91_{0.73}^{0.67}$	$2.50_{0.89}^{0.82}$
HDFS 1-107......	32 51.65	32 12.5	$1.00_{0.15}^{0.14}$	$0.79_{0.25}^{0.39}$	$0.46_{0.19}^{0.19}$	$0.37_{0.15}^{0.19}$
HDFS 1-99	32 55.75	32 13.6	$0.72_{0.12}^{0.13}$	$0.29_{0.13}^{0.17}$	$0.19_{0.08}^{0.10}$	$0.16_{0.06}^{0.09}$
HDFS 1-119......	32 52.01	32 15.0	$0.84_{0.13}^{0.13}$	$0.77_{0.31}^{0.35}$	$0.49_{0.19}^{0.23}$	$0.43_{0.16}^{0.21}$
HDFS 1-111......	32 54.82	32 15.4	$0.52_{0.11}^{0.11}$	$0.38_{0.21}^{0.41}$	$0.45_{0.24}^{0.33}$	$0.61_{0.31}^{0.35}$
HDFS 1-112......	32 54.42	32 15.4	$2.14_{0.23}^{0.22\,a}$	$4.15_{0.85}^{0.97}$	$2.35_{0.49}^{0.47}$	$1.79_{0.34}^{0.37}$
HDFS 1-113......	32 52.58	32 15.4	$1.50_{0.18}^{0.18}$	$1.45_{0.52}^{0.53}$	$1.08_{0.40}^{0.40}$	$1.08_{0.40}^{0.39}$
HDFS 1-117......	32 52.91	32 15.7	$1.54_{0.25}^{0.23}$	$0.44_{0.18}^{0.25}$	$0.39_{0.17}^{0.22}$	$0.48_{0.21}^{0.25}$
HDFS 1-115......	32 48.88	32 16.1	$0.54_{0.11}^{0.11}$	$0.26_{0.13}^{0.17}$	$0.19_{0.09}^{0.10}$	$0.18_{0.08}^{0.09}$
HDFS 1-127......	32 53.05	32 17.2	$0.78_{0.13}^{0.13}$	$0.60_{0.25}^{0.27}$	$0.37_{0.15}^{0.17}$	$0.31_{0.12}^{0.14}$
HDFS 1-121......	32 55.54	32 17.5	$0.48_{0.10}^{0.10}$	$0.22_{0.10}^{0.12}$	$0.14_{0.06}^{0.07}$	$0.11_{0.05}^{0.05}$
HDFS 1-125......	32 48.16	32 18.2	$1.40_{0.19}^{0.18}$	$0.68_{0.31}^{0.29}$	$0.50_{0.20}^{0.21}$	$0.49_{0.17}^{0.21}$
HDFS 1-131......	32 52.08	32 18.6	$1.38_{0.18}^{0.18\,a}$	$1.10_{0.43}^{0.44}$	$0.75_{0.28}^{0.30}$	$0.70_{0.24}^{0.29}$
HDFS 1-139......	32 47.80	32 19.7	$2.24_{0.23}^{0.25}$	$7.16_{1.69}^{1.93}$	$4.52_{0.89}^{1.42}$	$4.16_{0.83}^{1.22}$
HDFS 1-141......	32 56.08	32 20.4	$0.50_{0.11}^{0.11}$	$0.48_{0.23}^{0.28}$	$0.29_{0.15}^{0.15}$	$0.24_{0.11}^{0.12}$
HDFS 1-148......	32 50.50	32 22.6	$1.72_{0.23}^{0.22}$	$0.74_{0.30}^{0.38}$	$0.73_{0.30}^{0.33}$	$0.89_{0.33}^{0.38}$
HDFS 1-152......	32 52.01	32 24.4	$3.50_{0.35}^{0.33}$	$11.65_{1.83}^{2.88}$	$7.12_{1.18}^{2.31}$	$5.94_{0.73}^{4.15}$
HDFS 1-160......	32 49.16	32 26.2	$3.00_{0.28}^{0.28}$	$22.84_{3.03}^{4.28}$	$10.85_{0.72}^{1.58}$	$8.77_{0.43}^{1.18}$
HDFS 1-163......	32 48.44	32 28.7	$1.42_{0.17}^{0.17}$	$3.32_{1.35}^{1.18}$	$2.39_{0.89}^{0.85}$	$2.34_{0.76}^{0.84}$
HDFS 1-173......	32 53.52	32 31.9	$1.12_{0.15}^{0.18}$	$0.81_{0.27}^{0.41}$	$0.45_{0.16}^{0.22}$	$0.37_{0.12}^{0.21}$
HDFS 1-182......	32 46.79	32 33.7	$1.82_{0.24}^{0.21}$	$0.87_{0.41}^{0.40}$	$0.93_{0.39}^{0.38}$	$1.19_{0.45}^{0.44}$
HDFS 1-186......	32 53.66	32 35.9	$0.20_{0.08}^{0.09}$	$0.10_{0.08}^{0.16}$	$0.08_{0.06}^{0.11}$	$0.09_{0.06}^{0.12}$
HDFS 1-194......	32 48.37	32 38.0	$3.52_{0.33}^{0.32}$	$13.69_{2.73}^{2.61}$	$9.03_{1.80}^{3.12}$	$8.16_{1.55}^{5.88}$
HDFS 1-187......	32 53.34	32 39.1	$0.90_{0.13}^{0.13}$	$2.03_{0.85}^{0.97}$	$1.45_{0.59}^{0.81}$	$1.56_{0.58}^{0.75}$
HDFS 1-188......	32 53.12	32 39.1	$0.58_{0.11}^{0.11}$	$0.19_{0.09}^{0.11}$	$0.13_{0.06}^{0.06}$	$0.12_{0.05}^{0.06}$
HDFS 1-207......	32 50.89	32 43.1	$0.54_{0.11}^{0.11}$	$1.05_{0.66}^{0.92}$	$1.07_{0.57}^{0.71}$	$1.34_{0.64}^{0.75}$
HDFS 1-232......	32 54.06	32 51.7	$0.48_{0.10}^{0.10}$	$0.54_{0.26}^{0.31}$	$0.34_{0.16}^{0.17}$	$0.30_{0.13}^{0.14}$
HDFS 1-236......	32 47.65	32 52.4	$0.50_{0.11}^{0.10}$	$0.24_{0.11}^{0.15}$	$0.15_{0.07}^{0.08}$	$0.12_{0.05}^{0.06}$
HDFS 1-237......	32 49.24	32 53.5	$0.58_{0.11}^{0.11}$	$0.57_{0.26}^{0.33}$	$0.38_{0.18}^{0.18}$	$0.35_{0.15}^{0.17}$
HDFS 1-276......	32 51.18	33 01.4	$1.26_{0.16}^{0.16}$	$1.42_{0.51}^{0.46}$	$0.91_{0.33}^{0.30}$	$0.81_{0.28}^{0.27}$
HDFS 1-283......	32 47.04	33 02.9	$1.20_{0.17}^{0.15\,a}$	$1.02_{0.41}^{0.35}$	$0.65_{0.26}^{0.23}$	$0.58_{0.22}^{0.21}$
HDFS 1-286......	33 00.04	33 04.0	$1.24_{0.16}^{0.16\,a}$	$1.33_{0.44}^{0.36}$	$0.76_{0.24}^{0.23}$	$0.62_{0.20}^{0.18}$
HDFS 1-287......	32 57.26	33 05.4	$0.86_{0.13}^{0.13}$	$1.43_{0.58}^{0.58}$	$0.86_{0.33}^{0.40}$	$0.75_{0.28}^{0.34}$
HDFS 1-302......	32 54.02	33 05.4	$0.54_{0.11}^{0.11}$	$0.23_{0.14}^{0.19}$	$0.21_{0.11}^{0.13}$	$0.24_{0.11}^{0.12}$
HDFS 1-289......	32 57.59	33 06.1	$0.58_{0.11}^{0.11}$	$3.57_{1.61}^{2.24}$	$2.42_{1.16}^{1.15}$	$2.23_{0.92}^{1.10}$
HDFS 1-291......	32 51.68	33 06.1	$0.98_{0.14}^{0.14}$	$0.35_{0.17}^{0.33}$	$0.42_{0.19}^{0.27}$	$0.57_{0.25}^{0.28}$
HDFS 1-299......	32 52.30	33 08.3	$0.56_{0.11}^{0.11}$	$1.55_{0.75}^{0.97}$	$1.08_{0.52}^{0.56}$	$1.04_{0.45}^{0.51}$
HDFS 1-306......	32 48.05	33 09.4	$1.30_{0.17}^{0.16\,a}$	$0.81_{0.31}^{0.27}$	$0.51_{0.19}^{0.20}$	$0.46_{0.17}^{0.18}$
HDFS 1-313......	32 49.49	33 11.2	$0.52_{0.11}^{0.11}$	$0.27_{0.13}^{0.17}$	$0.17_{0.08}^{0.08}$	$0.15_{0.07}^{0.08}$
HDFS 1-317......	33 02.02	33 12.6	$0.78_{0.13}^{0.16\,a}$	$0.14_{0.07}^{0.11}$	$0.10_{0.04}^{0.07}$	$0.09_{0.04}^{0.07}$
HDFS 1-318......	32 53.92	33 13.3	$0.20_{0.08}^{0.08}$	$0.05_{0.03}^{0.10}$	$0.06_{0.04}^{0.10}$	$0.08_{0.06}^{0.11}$
HDFS 1-335......	33 04.00	33 13.7	$2.54_{0.26}^{0.26}$	$7.55_{1.50}^{1.44}$	$4.22_{0.87}^{1.08}$	$3.49_{0.75}^{0.97}$
HDFS 1-326......	32 48.55	33 14.0	$0.62_{0.12}^{0.13}$	$0.37_{0.15}^{0.25}$	$0.22_{0.10}^{0.12}$	$0.18_{0.07}^{0.10}$
HDFS 1-332......	33 01.94	33 16.2	$0.44_{0.10}^{0.10}$	$0.52_{0.28}^{0.36}$	$0.37_{0.19}^{0.22}$	$0.36_{0.17}^{0.19}$
HDFS 1-334......	32 52.91	33 16.9	$1.28_{0.16}^{0.16}$	$5.56_{2.58}^{2.53}$	$4.34_{1.71}^{1.95}$	$4.45_{1.44}^{1.99}$
HDFS 1-340......	32 55.90	33 17.6	$0.52_{0.11}^{0.11}$	$0.32_{0.15}^{0.20}$	$0.21_{0.10}^{0.10}$	$0.18_{0.08}^{0.09}$
HDFS 1-342......	33 00.18	33 18.7	$0.74_{0.12}^{0.12}$	$0.62_{0.25}^{0.26}$	$0.37_{0.14}^{0.15}$	$0.31_{0.11}^{0.12}$
HDFS 1-346......	32 54.31	33 20.2	$0.46_{0.11}^{0.10}$	$0.19_{0.10}^{0.13}$	$0.12_{0.06}^{0.07}$	$0.10_{0.05}^{0.05}$

TABLE 3—*Continued*

ID	R.A. (22$^{\rm h}$)	Decl. ($-60°$)	$z_{\rm phot}$	$L_U^{\rm rest}$ $(10^{10} L_\odot)$	$L_B^{\rm rest}$ $(10^{10} L_\odot)$	$L_V^{\rm rest}$ $(10^{10} L_\odot)$
HDFS 1-347	32 53.12	33 20.2	$3.28^{0.31a}_{0.33}$	$11.08^{1.64}_{1.60}$	$5.83^{0.82}_{0.48}$	$4.92^{1.15}_{0.36}$
HDFS 1-345	33 02.81	33 22.0	$0.56^{0.11}_{0.11}$	$2.29^{1.87}_{1.41}$	$2.09^{1.32}_{1.09}$	$2.43^{1.22}_{1.09}$
HDFS 1-350	33 05.00	33 22.0	$3.04^{0.33a}_{1.27}$	$9.39^{3.24}_{7.74}$	$7.60^{2.59}_{6.21}$	$8.04^{2.74}_{6.53}$
HDFS 1-355	32 54.24	33 22.3	$2.88^{0.34a}_{1.08}$	$3.61^{1.44}_{3.00}$	$2.80^{1.05}_{2.25}$	$2.88^{1.09}_{2.20}$
HDFS 1-354	32 57.26	33 23.0	$1.38^{0.24}_{0.19}$	$0.55^{0.38}_{0.24}$	$0.42^{0.27}_{0.17}$	$0.44^{0.27}_{0.17}$
HDFS 1-364	32 57.08	33 23.0	$0.68^{0.12}_{0.12}$	$0.94^{0.49}_{0.35}$	$0.53^{0.22}_{0.22}$	$0.43^{0.18}_{0.16}$
HDFS 1-363	32 52.15	33 23.8	$1.12^{0.15}_{0.15}$	$3.19^{1.26}_{1.22}$	$2.01^{0.84}_{0.77}$	$1.75^{0.77}_{0.66}$
HDFS 1-360	33 02.88	33 25.2	$1.30^{0.16}_{0.16}$	$5.26^{1.82}_{1.92}$	$3.52^{1.23}_{1.26}$	$3.25^{1.15}_{1.13}$
HDFS 1-368	33 00.94	33 25.6	$0.96^{0.14}_{0.14}$	$0.99^{0.49}_{0.36}$	$0.55^{0.29}_{0.20}$	$0.44^{0.26}_{0.17}$
HDFS 1-372	32 50.57	33 25.9	$0.56^{0.11}_{0.11}$	$0.49^{0.29}_{0.24}$	$0.33^{0.17}_{0.16}$	$0.32^{0.15}_{0.14}$
HDFS 1-373	32 50.71	33 25.9	$0.54^{0.11}_{0.11}$	$0.30^{0.19}_{0.15}$	$0.17^{0.12}_{0.08}$	$0.16^{0.10}_{0.07}$
HDFS 1-378	32 50.68	33 28.4	$2.62^{0.25}_{0.38}$	$19.36^{4.57}_{5.42}$	$11.99^{2.83}_{3.78}$	$10.14^{2.39}_{2.98}$
HDFS 1-379	32 53.05	33 28.4	$1.06^{0.14}_{0.15}$	$3.15^{2.09}_{1.41}$	$2.82^{1.46}_{1.28}$	$3.31^{1.33}_{1.38}$
HDFS 1-377	32 55.00	33 28.8	$1.12^{0.15}_{0.15}$	$1.37^{0.95}_{0.65}$	$1.46^{0.70}_{0.63}$	$1.89^{0.66}_{0.75}$
HDFS 1-380	32 57.12	33 28.8	$0.68^{0.12}_{0.12}$	$0.11^{0.09}_{0.06}$	$0.12^{0.08}_{0.06}$	$0.16^{0.09}_{0.08}$
HDFS 1-381	32 59.50	33 28.8	$1.00^{0.14}_{0.15}$	$0.68^{0.30}_{0.24}$	$0.40^{0.20}_{0.15}$	$0.33^{0.18}_{0.13}$
HDFS 1-382	32 58.31	33 29.2	$2.62^{0.26}_{0.26}$	$5.48^{1.41}_{1.19}$	$3.44^{0.90}_{0.74}$	$2.95^{0.79}_{0.62}$
HDFS 1-386	33 03.24	33 29.5	$2.64^{0.25}_{0.26}$	$22.52^{5.21}_{4.13}$	$13.77^{3.17}_{2.96}$	$11.50^{2.63}_{2.22}$
HDFS 1-383	32 58.24	33 31.3	$0.42^{0.10}_{0.10}$	$0.48^{0.33}_{0.25}$	$0.31^{0.18}_{0.16}$	$0.28^{0.15}_{0.14}$
HDFS 1-424[b]	32 56.83	33 31.7	$4.82^{0.41}_{0.41}$	$28.02^{10.54}_{6.91}$	$24.97^{6.74}_{11.23}$	$31.13^{7.16}_{18.65}$
HDFS 1-393	33 01.80	33 31.7	$1.62^{0.20}_{0.19}$	$4.21^{1.52}_{1.35}$	$2.96^{1.07}_{1.02}$	$2.85^{1.04}_{1.00}$
HDFS 1-394	33 04.28	33 31.7	$0.10^{0.35}_{0.08}$	$0.00^{0.13}_{0.00}$	$0.00^{0.09}_{0.00}$	$0.00^{0.08}_{0.00}$
HDFS 1-395	32 54.71	33 33.1	$0.16^{0.08}_{0.08}$	$0.07^{0.12}_{0.05}$	$0.05^{0.08}_{0.04}$	$0.05^{0.08}_{0.04}$
HDFS 1-397	32 53.41	33 33.1	$1.10^{0.22}_{0.15}$	$1.20^{1.33}_{0.50}$	$1.00^{0.88}_{0.42}$	$1.11^{0.78}_{0.41}$
HDFS 1-399	32 52.37	33 33.1	$0.52^{0.11}_{0.12}$	$0.37^{0.24}_{0.18}$	$0.24^{0.12}_{0.12}$	$0.22^{0.11}_{0.10}$
HDFS 1-404	32 55.75	33 33.5	$0.54^{0.11}_{0.11}$	$0.24^{0.14}_{0.10}$	$0.15^{0.07}_{0.07}$	$0.12^{0.06}_{0.05}$
HDFS 1-405	33 00.04	33 33.8	$1.02^{0.14}_{0.14}$	$0.30^{0.23}_{0.14}$	$0.36^{0.19}_{0.16}$	$0.49^{0.20}_{0.21}$
HDFS 1-398	32 53.30	33 34.9	$0.96^{0.17a}_{0.16}$	$0.17^{0.18}_{0.10}$	$0.18^{0.14}_{0.09}$	$0.23^{0.14}_{0.11}$
HDFS 1-406	32 47.65	33 36.0	$0.58^{0.11}_{0.11}$	$4.83^{3.83}_{2.83}$	$4.38^{2.70}_{2.23}$	$5.08^{2.49}_{2.23}$
HDFS 1-411	32 54.96	33 36.7	$1.00^{0.15}_{0.14}$	$0.30^{0.22}_{0.12}$	$0.26^{0.16}_{0.11}$	$0.31^{0.14}_{0.13}$
HDFS 1-427	33 02.88	33 37.1	$1.18^{0.23}_{0.18}$	$0.59^{0.54}_{0.24}$	$0.44^{0.34}_{0.20}$	$0.46^{0.30}_{0.19}$
HDFS 1-414	32 51.50	33 37.4	$0.62^{0.11}_{0.11}$	$0.86^{0.50}_{0.44}$	$0.65^{0.33}_{0.30}$	$0.66^{0.31}_{0.27}$
HDFS 1-410	32 53.77	33 37.4	$0.52^{0.11}_{0.11}$	$1.03^{0.67}_{0.49}$	$0.66^{0.33}_{0.33}$	$0.59^{0.31}_{0.26}$
HDFS 1-415	32 59.46	33 39.6	$0.46^{0.10}_{0.10}$	$0.49^{0.29}_{0.25}$	$0.32^{0.17}_{0.16}$	$0.29^{0.15}_{0.13}$
HDFS 1-421	33 03.64	33 41.4	$0.44^{0.10}_{0.10}$	$1.76^{1.43}_{1.00}$	$1.43^{0.95}_{0.77}$	$1.55^{0.82}_{0.77}$
HDFS 1-426	32 54.02	33 41.4	$1.00^{0.14}_{0.15}$	$0.59^{0.39}_{0.27}$	$0.48^{0.27}_{0.21}$	$0.56^{0.23}_{0.24}$
HDFS 1-434	32 49.45	33 43.9	$0.58^{0.12}_{0.11}$	$0.13^{0.10}_{0.06}$	$0.09^{0.06}_{0.04}$	$0.09^{0.05}_{0.04}$
HDFS 1-435	32 47.47	33 44.3	$0.56^{0.11}_{0.11}$	$0.10^{0.07}_{0.05}$	$0.08^{0.05}_{0.04}$	$0.08^{0.04}_{0.04}$
HDFS 1-437	32 49.99	33 45.0	$1.06^{0.14}_{0.15}$	$1.35^{0.56}_{0.42}$	$0.74^{0.26}_{0.30}$	$0.58^{0.25}_{0.23}$
HDFS 1-439	33 02.52	33 46.4	$0.68^{0.12}_{0.12}$	$1.38^{0.66}_{0.59}$	$0.83^{0.35}_{0.34}$	$0.68^{0.29}_{0.26}$
HDFS 1-440	32 58.63	33 46.4	$1.34^{0.16}_{0.17}$	$0.82^{0.50}_{0.33}$	$1.03^{0.47}_{0.39}$	$1.41^{0.55}_{0.53}$
HDFS 1-448	32 45.56	33 47.2	$1.30^{0.16}_{0.16}$	$2.35^{0.59}_{0.74}$	$1.34^{0.35}_{0.40}$	$1.08^{0.27}_{0.33}$
HDFS 1-450	32 57.88	33 49.0	$0.44^{0.10}_{0.10}$	$0.11^{0.07}_{0.06}$	$0.07^{0.04}_{0.04}$	$0.07^{0.03}_{0.03}$
HDFS 1-463	33 03.10	33 53.3	$2.76^{0.28}_{0.50}$	$4.26^{1.25}_{1.22}$	$3.31^{1.07}_{1.24}$	$3.53^{1.25}_{1.55}$
HDFS 1-484	32 46.90	33 54.7	$0.52^{0.11}_{0.11}$	$0.55^{0.56}_{0.32}$	$0.63^{0.45}_{0.33}$	$0.85^{0.49}_{0.43}$
HDFS 1-472	32 48.26	33 55.1	$0.66^{0.12}_{0.12}$	$0.36^{0.20}_{0.17}$	$0.25^{0.12}_{0.11}$	$0.24^{0.11}_{0.10}$
HDFS 1-476	33 00.90	33 56.9	$1.08^{0.15}_{0.15}$	$1.03^{0.41}_{0.37}$	$0.61^{0.26}_{0.23}$	$0.50^{0.23}_{0.20}$
HDFS 1-480	32 53.02	33 56.9	$2.76^{0.53a}_{0.66}$	$1.43^{1.54}_{0.85}$	$1.79^{1.73}_{1.06}$	$2.47^{2.25}_{1.46}$
HDFS 1-479	32 59.24	33 57.2	$1.34^{1.77a}_{0.17}$	$1.16^{11.35}_{0.48}$	$0.84^{8.05}_{0.32}$	$0.81^{7.82}_{0.27}$
HDFS 1-483	33:2.74	33 58.0	$2.24^{0.31}_{0.23}$	$6.19^{1.90}_{1.36}$	$3.84^{1.27}_{0.79}$	$3.37^{1.05}_{0.67}$
HDFS 1-487	32 51.54	33 58.3	$1.28^{0.16a}_{0.24}$	$0.28^{0.15}_{0.17}$	$0.27^{0.12}_{0.14}$	$0.32^{0.13}_{0.16}$
HDFS 1-488	32 52.15	33 59.4	$0.48^{0.14}_{0.10}$	$0.44^{0.53}_{0.23}$	$0.35^{0.34}_{0.18}$	$0.37^{0.29}_{0.17}$
HDFS 1-492	32 51.32	34 01.6	$0.24^{0.90a}_{0.12}$	$0.02^{0.81}_{0.02}$	$0.01^{0.46}_{0.01}$	$0.01^{0.36}_{0.01}$
HDFS 1-489	32 52.26	34 02.6	$0.52^{0.11}_{0.11}$	$0.48^{0.49}_{0.26}$	$0.37^{0.37}_{0.20}$	$0.40^{0.20}_{0.19}$
HDFS 1-478	32 50.96	34 04.8	$1.34^{0.16}_{0.17}$	$5.12^{1.83}_{2.03}$	$3.37^{1.36}_{1.19}$	$3.17^{1.27}_{1.03}$
HDFS 1-505	32 59.86	34 05.5	$1.30^{0.16}_{0.17}$	$1.92^{0.76}_{0.76}$	$1.33^{0.54}_{0.52}$	$1.27^{0.52}_{0.48}$
HDFS 1-511	32 49.85	34 06.2	$1.12^{0.15}_{0.15}$	$2.43^{1.11}_{1.01}$	$1.64^{0.79}_{0.64}$	$1.52^{0.78}_{0.53}$
HDFS 1-516	32 55.28	34 07.7	$0.46^{0.10}_{0.10}$	$0.33^{0.19}_{0.16}$	$0.20^{0.10}_{0.09}$	$0.16^{0.08}_{0.07}$
HDFS 1-542	32 51.11	34 08.0	$3.86^{0.34a}_{3.46}$	$31.10^{6.03}_{31.03}$	$15.42^{1.61}_{15.36}$	$12.60^{1.02}_{12.55}$
HDFS 1-521	32 47.58	34 08.8	$0.50^{0.11}_{0.11}$	$0.89^{0.67}_{0.48}$	$0.67^{0.43}_{0.36}$	$0.69^{0.36}_{0.33}$
HDFS 1-522	33 04.50	34 08.8	$0.56^{0.11}_{0.11}$	$0.15^{0.09}_{0.07}$	$0.10^{0.05}_{0.05}$	$0.09^{0.04}_{0.04}$
HDFS 1-530	32 55.25	34 10.2	$1.02^{0.14}_{0.14}$	$1.36^{0.60}_{0.52}$	$0.90^{0.37}_{0.37}$	$0.83^{0.36}_{0.32}$
HDFS 1-536	33 01.58	34 10.6	$0.78^{0.13}_{0.13}$	$0.58^{0.28}_{0.25}$	$0.37^{0.18}_{0.15}$	$0.33^{0.16}_{0.13}$
HDFS 1-527	33 01.80	34 13.4	$1.12^{0.15}_{0.15}$	$3.83^{2.51}_{1.67}$	$3.59^{1.74}_{1.55}$	$4.33^{1.56}_{1.71}$
HDFS 1-538	32 56.11	34 14.2	$0.52^{0.11}_{0.11}$	$0.66^{0.43}_{0.30}$	$0.42^{0.22}_{0.21}$	$0.37^{0.19}_{0.16}$
HDFS 1-548	33 00.54	34 17.4	$0.66^{0.12}_{0.12}$	$0.19^{0.17}_{0.10}$	$0.23^{0.15}_{0.11}$	$0.30^{0.17}_{0.14}$
HDFS 1-555	32 59.60	34 20.3	$1.12^{0.15}_{0.15}$	$0.98^{0.63}_{0.51}$	$1.02^{0.50}_{0.43}$	$1.28^{0.52}_{0.46}$

Note.—Units of right ascension are minutes and seconds, and units of declination are arcminutes and arcseconds (J2000).

[a] Here $\geq 1\%$ of Monte Carlo realizations have z more than unity away from $z_{\rm phot}$.

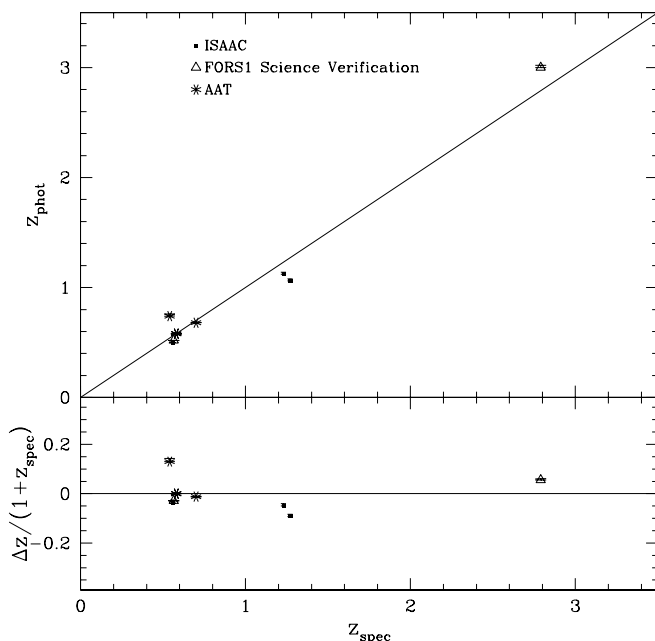[b] The value of $z_{\rm phot}$ may be discrepant.

FIG. 4.—Comparison of z_{phot} to z_{spec} for objects in the WFPC2 field of the HDF-S. The explanation of this figure is identical to Fig. 3. The values of δz_{phot} are derived from a Monte Carlo simulation using the formal photometric errors. Two objects with $z_{spec} = 0.58$ measurements from the AAT both have values of $z_{phot} = 0.58$.

mates were obviously wrong. In both of these cases, the inclusion of the NIR data forces the code to incorrectly identify a LB just entering the F300W band as a rest-frame optical break. When leaving out these two galaxies, Δz at $z_{spec} > 1.9$ remains unchanged by the omission of the NIR data. We should expect that the NIR data should improve the accuracy of the redshifts, but it is possible that the flux errors in the NIR have been underestimated by FLY99 and that these data may overly contribute to the χ^2. Unfortunately, the importance of the NIR data cannot be assessed in the redshift range $1.3 < z < 2$ because of the lack of spectroscopic redshifts. In this regime, however, only rest-frame optical breaks are observable, and the NIR data is needed to constrain their position.

3.3.2. Hubble Deep Field South

For the HDF-S, we selected all the objects in our catalog with publicly available spectroscopic redshifts. These include five objects detected by ISOCAM (Rigopoulou et al. 2000) with spectroscopic redshifts from ISAAC, two objects from the FORS1 commissioning data (Cristiani et al. 2000), and four objects with unpublished spectra taken with the Anglo-Australian Telescope (AAT; Glazebrook 2001, hereafter G01),[12] all of which lie in our area with "good photometry." Two of the objects from G01 also had spectra from Rigopoulou et al. (2000) that yielded identical values of z_{spec}. The comparison of our z_{phot} to z_{spec} for these objects is shown in Figure 4. We find excellent agreement between z_{phot} and z_{spec} with $\Delta z \approx 0.05$ and 0.18 for $z \leq 1.0$ and $z > 1.0$, respectively.

3.3.3. Template Mismatch and Redshift Uncertainties

The photometric redshift error bars derived solely from the Monte Carlo simulation described in § 3.2 significantly underestimate the true variance of z_{phot} when compared to

---

[12] Available at http://www.aao.gov.au/hdfs.

z_{spec}. This is because the galaxies with spectroscopic redshifts are among the brightest galaxies in our sample, with very small formal flux errors. The resulting range of statistically acceptable redshifts and SEDs is very small, and our coarse and finite set of templates significantly distorts z_{spec} but is not modeled by our Monte Carlo estimates. At the faint end, the photometric errors become large and dominate the uncertainty in the redshift, implying realistic error estimates. Both effects were noted by FLY99.

We first attempted to compensate for this "template mismatch" in the bright galaxies by using a minimum photometric error of 10% chosen such that our Monte Carlo error bars reflect the deviation of z_{phot} from z_{spec}. By introducing a minimum flux error, we lessen the relative contribution of the high signal-to-noise *HST* data points to the χ^2 budget—which in turn changes the formal best-fit redshift. A detailed examination of this effect in the HDF-N and HDF-S data showed that while this minimum photometric error brought the z_{phot} values into statistical agreement with z_{spec}, the actual best-fit values of z_{phot} agreed worse with z_{spec} than when using the formal photometric errors. In fact, $\sim 20\%$ of the galaxies in both the HDF-N and HDF-S have z_{phot} values calculated with the formal flux errors, which lie outside the 68% confidence limits allowed with the boosted flux errors.

Hence, a proper estimate of the uncertainty in z_{phot} must take into account both systematic uncertainties arising from template mismatch and the uncertainties in z_{phot} that result from the formal photometric errors. We define the total uncertainty in z_{phot} as

$$\delta z_{phot} \equiv \sqrt{\langle |\Delta z| \rangle^2 + \delta z_{MC}^2} , \qquad (5)$$

where $\langle |\Delta z| \rangle$ is the value of $(1 + z_{phot})$ times the mean value of $\Delta z/(1 + z) = 0.07$ as derived from the HDF-N, and δz_{MC} is again the 68% confidence limit of z_{phot} as derived from the Monte Carlo simulation. Note that δz_{MC} need not be symmetric around z_{phot}, and that we add Δz in quadrature separately for the upper and lower error bars. Again, the values of δz_{phot} are listed in Table 3.

In addition to providing realistic error bars, it is also informative to flag objects with secondary minima in their $\chi^2(z)$ distributions. Although some secondary minima in $\chi^2(z)$ are reflected by large values of δz_{MC}, some objects with small δz_{MC} may have a finite fraction of the Monte Carlo realizations that end up at a rather different redshift. In fact, some of the objects with large Δz in the HDF-N have secondary minima close to z_{spec} that are too small to be included in δz_{MC}. In addition to supplying the error bars that define the range of a galaxy's most likely redshifts, we flag in Table 3 the 20 objects for which $\geq 1\%$ of the Monte Carlo realizations lie greater than unity in redshift away from z_{phot}.

4. RESULTS

In the section below, we use our estimates of z_{phot} to examine the redshift distribution of galaxies in the HDF-S. We also use our estimate of z_{phot}, coupled with our broad wavelength coverage, to determine the rest-frame optical SEDs and luminosities of our galaxies across a wide range in redshift.

4.1. SED Fits

In Figure 5, we show 10 examples of SED fits to the seven-band photometry (0.3–2.2 μm) for galaxies in the
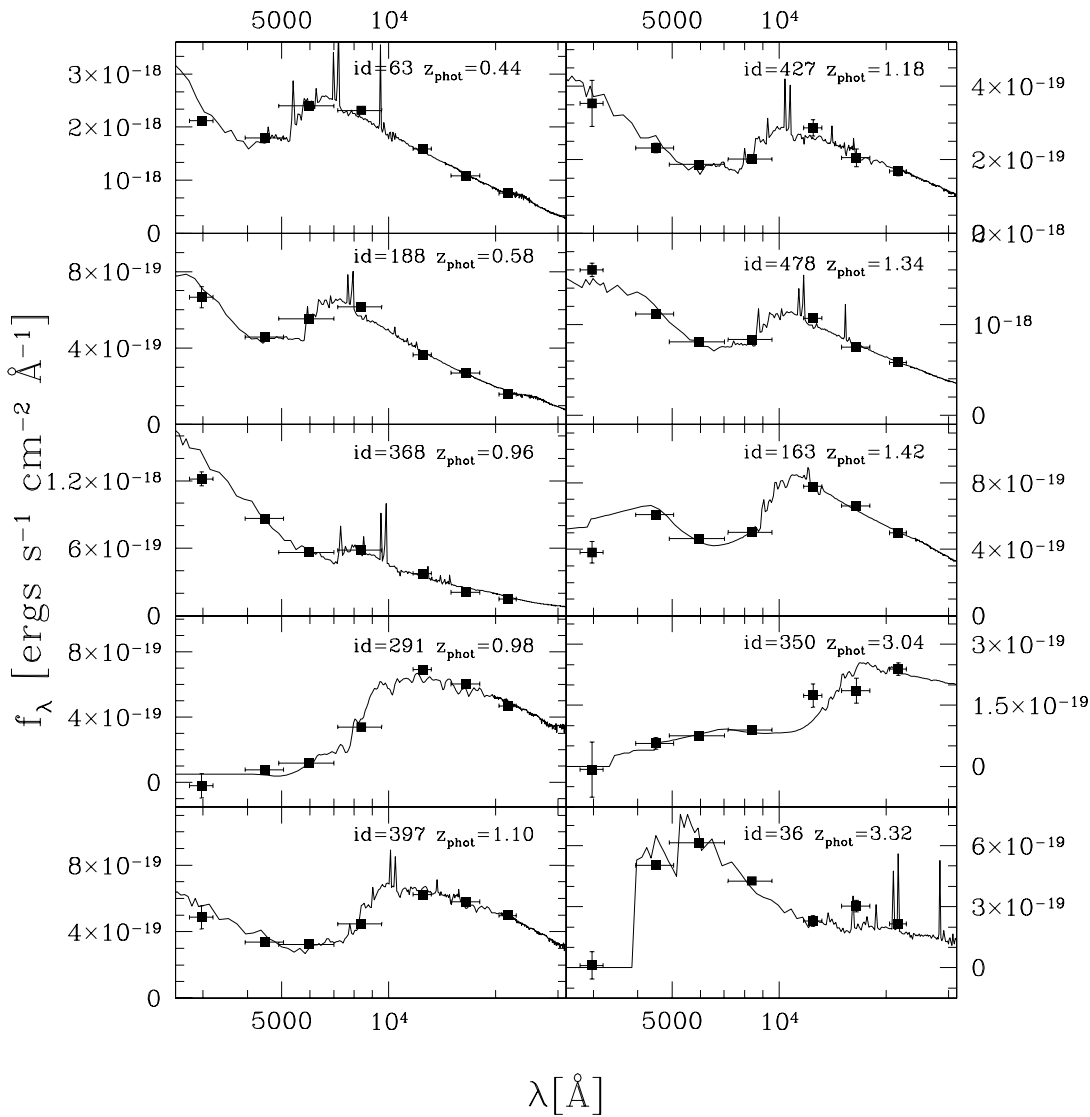
Fig. 5.—Sample of template fits to photometric data for 10 objects in the HDF-S. The measured z_{phot} increases down and to the right. In addition to blue, star-forming galaxies, there are many galaxies at $z > 1$ with strong Balmer or 4000 Å breaks.

HDF-S. In our analysis of K_s-band–selected galaxies in the HDF-S, we find galaxies with a range of SEDs at all redshifts $0 < z < 3$ with SED shapes ranging from very blue starburst templates to earlier Hubble type templates. As is shown in Figure 5, we also find galaxies with strong rest-frame 4000 Å breaks or Balmer breaks at $z > 1$. These breaks signal that the rest-frame optical light is dominated by stars at least as old as A stars. Note that the small flux errors of the F606W and F814W data force the best-fit SED at any redshift to always pass through these two points. This is best shown in Figure 6, where for each of our 136 galaxies, we plot the fractional difference between the measured flux and the model flux of our best-fit SED as a function of $K_{s,AB}$. At all magnitudes, the residuals are lowest in the F606W and F814W bands, even if they are very large in other bands. This plot is also useful for finding systematic differences between the SEDs and the data. For example, it is seen that the best-fit SED slightly overpredicts the F300W flux at all magnitudes.

To demonstrate the effect of the inclusion of deep NIR data in the redshift range $1.5 < z < 2$, we show in Figure 7

two galaxies fit with and without the NIR information. Even where the $V - I$ color is well constrained and hence the possible redshifts severely limited, the NIR data can fix the break position.

The three highest redshift objects in our sample (objects 542, 424, and 45) have $z_{phot} = 3.86$, 4.82, and 5.34 and $K_{s,AB}^{tot} = 22.75$, 23.29, and 23.16, respectively. Object 542 has 68% redshift confidence limits of $z_{phot} = 0.42$–3.88. In general, while the observed SED of object 424 is fitted well, there is flux blueward of the predicted 912 Å break position. The high redshift is chosen by the technique because the red $H - K_s$ color indicates the presence of a rest-frame optical break. No Monte Carlo realizations end up in a secondary minimum, but when fit using only the optical data, a redshift of 1.1 is found. Object 45 has a poor fit in the NIR and has a redshift of 1.34 when fitted with only the optical data. We do not consider these objects in any of our analyses.

4.2. Redshift Distribution

In Figure 8, we show the histogram of the photometric redshifts listed in Table 3. The three sets of lines represent
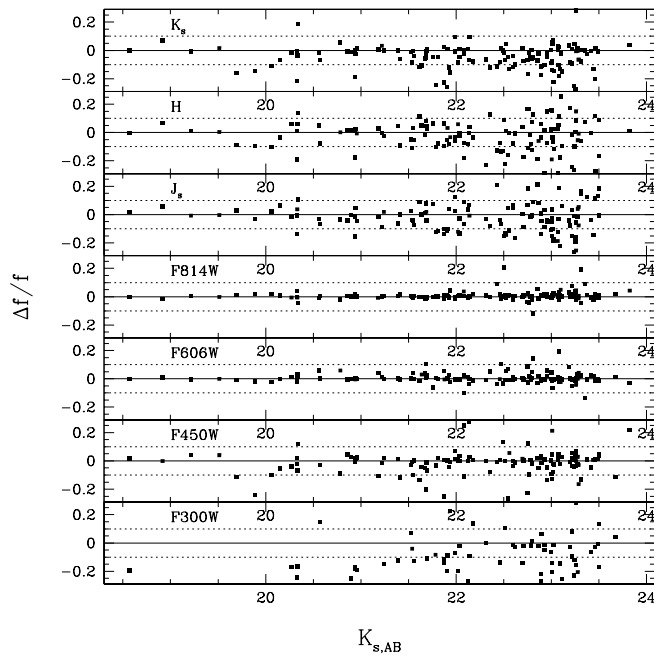
FIG. 6.—Fractional difference between the observed and model fluxes at the best-fit redshift as a function of $K_{s,AB}$. The horizontal dotted lines are at $\pm 10\%$ to guide the eye. The high signal-to-noise ratio of the F814W and F606W data forces the best-fit SED to always pass close to these points.

FIG. 8.—Redshift histogram of all 133 objects in our catalog with reliable redshifts (solid line). The two other histograms show the redshift distributions for all objects with $\delta z_{phot} \leq 0.4$ (dashed line) and all objects with $\delta z_{phot} \leq 0.2$ (dotted line), where the photometric redshift errors are the combination of those calculated using our Monte Carlo technique with the systematic errors determined from the HDF-N.

galaxies with different photometric redshift precision. This figure also reveals structure in the redshift histogram with a sharp peak at $z_{phot} \approx 0.5$ and a broad enhancement at $1 \leq z_{phot} \leq 1.4$. The redshift peak at $z \approx 0.5$ was first noticed by G01 from AAT spectroscopic redshifts taken over a larger field centered on the HDF-S. To examine the luminosity distribution of galaxies in these enhancements, we plot z_{phot} versus $K_{s,AB}^{tot}$ in Figure 9, revealing that they are prominent

in very bright galaxies; $K_{s,AB}^{tot} < 21.5$. These strong features in our redshift distribution are also seen in a $K_{s,AB}^{tot} \leq 23.5$ subsample of the HDF-S data from Fontana et al. (2000). HDF-N contains several peaks, but they are not as strong as the features in the HDF-S (Cohen et al. 1996).

We can use the overall redshift distribution of galaxies in our sample to test the predictions of theoretical models of
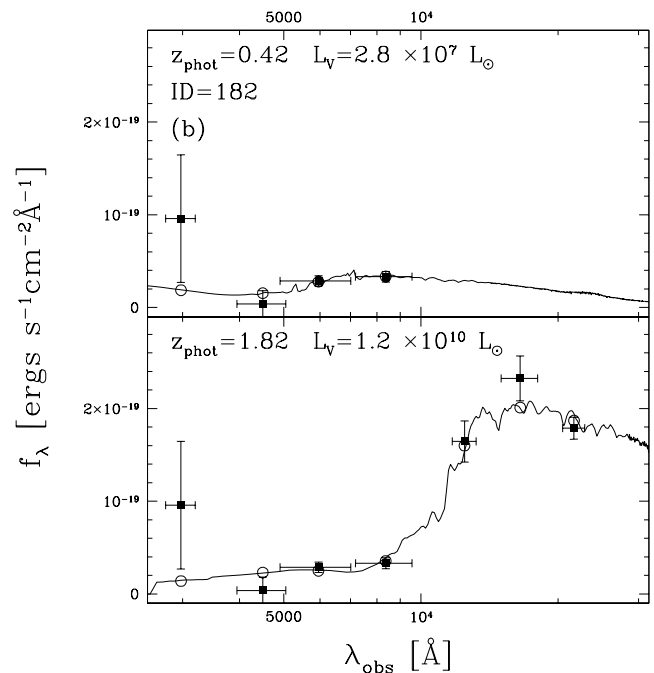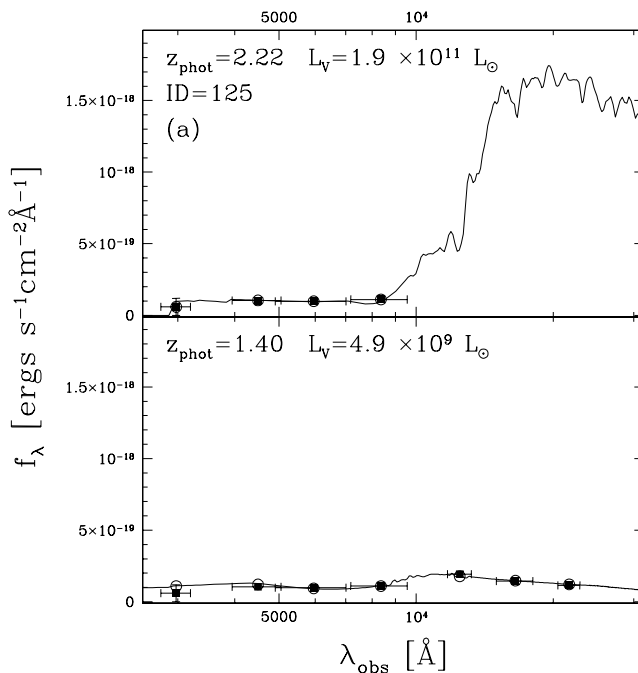
FIG. 7.—Two examples of how the inclusion of NIR data helps to measure the correct z_{phot}. Obviously, the inferred L^{rest} is strongly coupled to z_{phot}. The top panels for each object contain the fit using only data from the four optical *HST* filters. The bottom panels contain the fit using all seven bands. The filled squares are the data, and the open circles are the model fluxes.
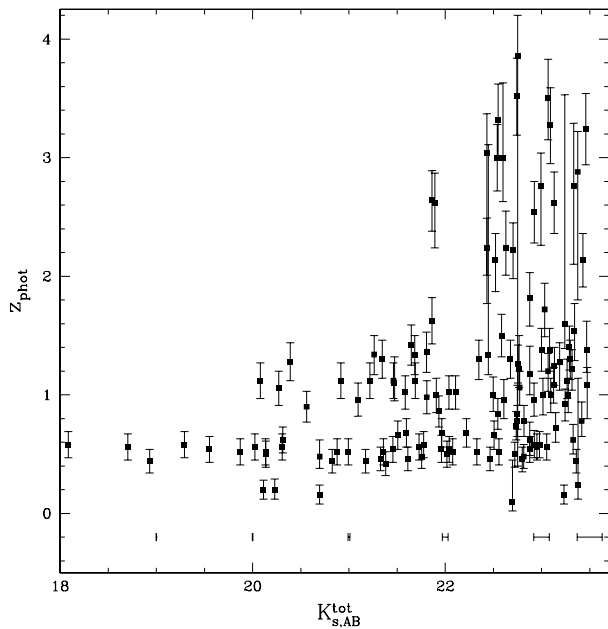
FIG. 9.—$K_{s,AB}^{tot}$ magnitude of our objects vs. z_{phot}. The photometric redshift errors are a combination of those calculated using our Monte Carlo technique and the systematic errors calculated from agreement with spectroscopic redshifts in the HDF-N. At the bottom of the graph, we show the typical photometry errors of objects of different magnitude.

galaxy formation. In Figure 10, we directly compare our cumulative redshift distribution for galaxies with $K_{s,vega} < 21$ to the theoretical predictions for SCDM ($\Omega_m = 1.0$, $\Lambda = 0.0$, and $h = 0.5$), ΛCDM ($\Omega_m = 0.3$, $\Lambda = 0.7$, and $h = 0.6$), and pure luminosity evolution (PLE) models cal-
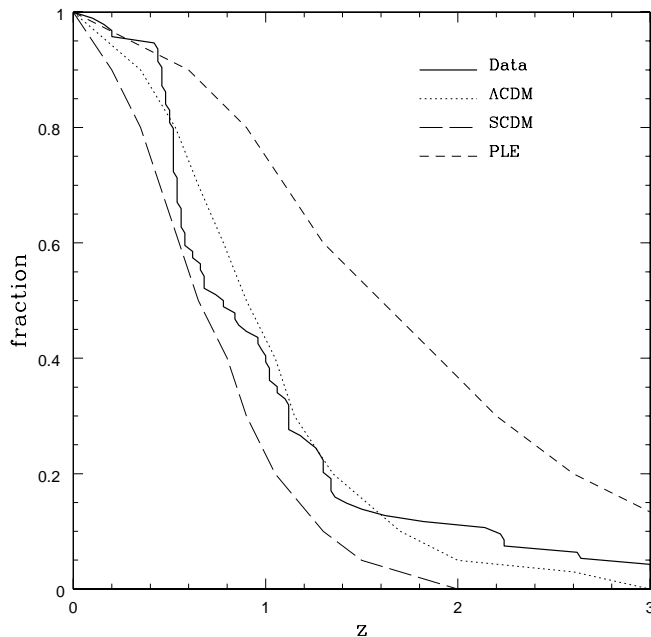
FIG. 10.—Cumulative redshift histogram for the 95 galaxies in our sample with $K_{s,vega} < 21$, as indicated by the solid line. The other lines are semianalytical model predictions from Fontana et al. (1999) for an SCDM ($\Omega_m = 1.0$, $\Lambda = 0.0$, $h = 0.5$; long-dashed line), ΛCDM ($\Omega_m = 0.3$, $\Lambda = 0.7$, $h = 0.6$; dotted line), and PLE model (short-dashed line). The data are generally consistent with hierarchical models of formation, while the PLE model significantly overpredicts the number of bright galaxies at high redshift.

culated by F99, following slightly modified versions of the KC98 prescriptions. At almost all redshifts, SCDM underpredicts the fraction of galaxies that lie at high redshifts, while the ΛCDM model provides a much better description of the data. Both CDM models reproduce the median redshift of the data ($z \sim 0.8$) reasonably well. The difference between the CDM models can be understood because galaxy formation occurs at higher redshift in a Λ-dominated universe. It is also interesting to note that the PLE models severely overpredict the abundance of bright galaxies at all redshifts. Our data has a low ($\lesssim 1\%$) Kolmogorov-Smirnov probability of being drawn from any of the models. This is likely due to the clustering of galaxies in our small volume, since the CDM models reproduce the general trends well. We note, however, that the models do not take into account any of the observational biases or the incompleteness that may occur for IR-selected galaxies. NIR selection is generally thought to be less prone to extinction effects and less dependent on the current SFR than optical selection. However, surface brightness dimming and the bright IR sky can limit detection efficiency for extended objects.

We now compare our results directly with those of F99 and the SUNY group. F99 claims that in a $K_{s,vega} < 21$ sample, only 2% of the galaxies lie at $z_{phot} \geq 2$ in the HDF-S and 6% in the NTT Deep Field. In contrast, we find in our data that 12% of the galaxies with $K_{s,vega} < 21$ lie at $z_{phot} \geq 2$. Using a $K_{s,vega} < 21$ subsample of the SUNY Stony Brook HDF-S photometric redshift catalog, we find that the fraction of galaxies lying at $z_{phot} \geq 2$ is identical to ours. The differences between us and F99 are not due to small sample selection issues. There are five galaxies with $K_{s,vega} < 21$ that F99 place at $1.5 < z < 2$ but that we find at $2 < z < 3$. The exact differences between the high-redshift fractions measured by different photometric redshift techniques can depend rather sensitively on the redshift threshold used to discriminate between "high" and "low" redshift galaxies. For example, although there is disagreement on the fraction of galaxies at $z_{phot} \geq 2$, both F99 and we are in agreement about the fraction of the $K_{s,vega} < 21$ galaxies ($\sim 14\%$–15%) in the HDF-S that lie at $z_{phot} \geq 1.5$. These discrepancies will be eventually resolved with extensive spectroscopy in the NIR and the blue optical.

4.3. Rest-Frame Luminosities

Our long wavelength baseline allows us to observe a given rest-frame wavelength over a large range in redshift. From the best-fit SED at the best-fit redshift, we measured the rest-frame luminosity in the U, B, and V bands for our galaxies and plot this as a function of enclosed volume and redshift in Figure 11. As reference to solar values, we take 2.73×10^{29}, 5.10×10^{29}, and 4.94×10^{29} ergs s^{-1} Å^{-1} for $L_\odot^U$, $L_\odot^B$, and $L_\odot^V$, respectively (assuming $M_U = +5.66$, $M_B = +5.47$, and $M_V = +4.82$ in Johnson magnitudes; Cox 2000). Using the distribution of L^{rest} values measured over δz_{phot}, we calculate an error bar in L^{rest} for each galaxy. While we differentiate points in Figure 11 based on their values of δz_{phot}, the errors in L^{rest} are tightly coupled with the values of δz_{phot} and so are not presented on this plot. This coupling is demonstrated by the two cases in Figure 7 where the main uncertainty in L^{rest} stems from the uncertainty in z_{phot}, not from the specific values of the NIR data. All values of L^{rest} and their associated uncertainties are presented in Table 3.
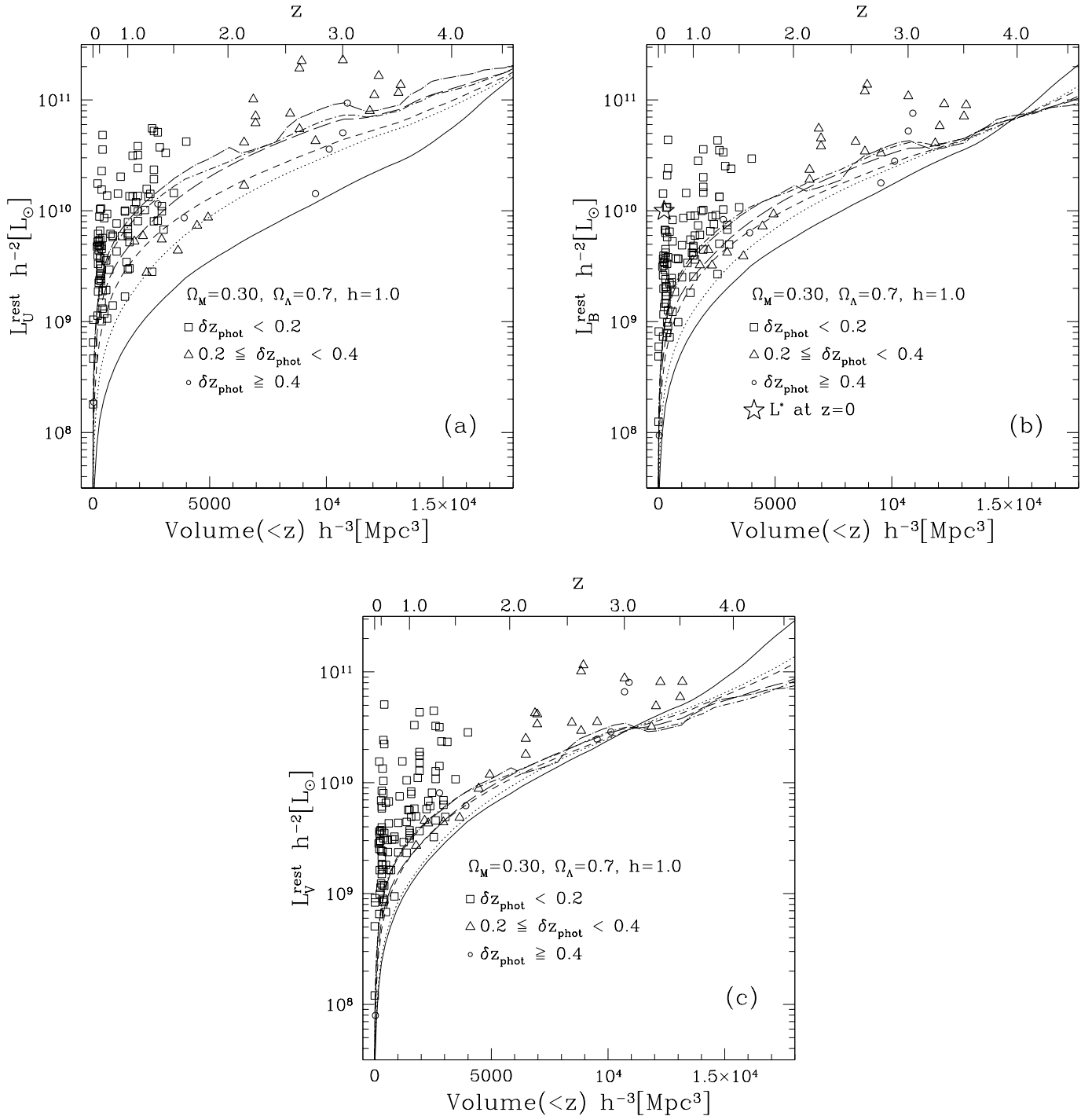
FIG. 11.—Distribution of rest-frame U-, B-, and V-band luminosities as a function of enclosed comoving volume and z_{phot} shown in (a), (b), and (c), respectively. We show all 133 galaxies with $K_{s,AB} \leq 23.5$ and reliable redshift estimates. Note the large number of galaxies at $z_{phot} \geq 2$ with $L^{rest} \geq 5 \times 10^{10}$ $L_{\odot}$. The tracks represent the values of L^{rest} for each our six template spectra normalized at each redshift to $K_{s,AB} = 23.5$. The large star in (b) indicates the value of L_B^* from local surveys. The specific tracks correspond to the E (solid line), Sbc (dotted line), Scd (short-dashed line), Irr (long-dashed line), SB1 (dot–short-dashed line), and SB2 (dot–long-dashed line) templates.

Because our fluxes are measured in uncorrected 2″0 apertures, we may be missing flux for the larger galaxies. Therefore, we correct all values of L^{rest} by the ratio (in the K_s band) of the SExtractor total flux to the 2″0 aperture flux. The median correction factor is 1.05 with 68% confidence limits of 0.97 and 1.25. The largest correction is by a factor of 1.72. To quantitatively assess the goodness of our SED fits, we compared the luminosities derived from the best-fit

SED to the luminosities derived from a linear interpolation between the observed filters shifted to the desired redshift and found the rms differences to be $\lesssim 10\%$ in all bands.

Perhaps the most interesting feature of Figure 11 is the presence of intrinsically luminous galaxies ($L^{rest} \geq 5 \times 10^{10}$ $h^{-2} L_{\odot}$) in all passbands at high redshifts. The apparent lack of low-luminosity galaxies at high redshift in Figure 11 merely reflects our K_s magnitude limit translated to a rest-

frame luminosity limit. Also apparent in Figure 11, at $z > 1$, is the increasing range in L^{rest} toward shorter rest-frame wavelengths. This is due to our magnitude limit in K_s, combined with the variation in intrinsic galaxy colors. We demonstrate this by showing the L^{rest}-z tracks of our six galaxy templates normalized to $K_{s,AB} = 23.5$.

We use the local B-band luminosity function to estimate the evolution in the bright high-redshift galaxies. We find nine galaxies with $L_B^{rest} \geq 5 \times 10^{10} \ h^{-2} \ L_{\odot,B}$ that lie in a volume of $7.29 \times 10^3 \ h^{-3} \ Mpc^3$ between $2 \leq z \leq 3.5$. We should be at least 50% complete for all galaxy types over this redshift and luminosity range. The number of galaxies at the bright end of the luminosity function is especially sensitive to variations in L^*, and we try to measure evolution in the luminosity function by holding α and ϕ^* constant and changing L^* to match the observed counts. We use the local luminosity functions derived from the Sloan Digital Sky Survey (SDSS; Blanton et al. 2001) and the 2dF Galaxy Redshift Survey (2dFGRS; Folkes et al. 1999) to predict the number of galaxies expected in this volume. The 2dFGRS luminosity function is in b_j magnitudes, and Blanton et al. (2001) provide a conversion of their SDSS luminosity function to this system. With $B = b_j + 0.2$ for a typical galaxy color of $(B - V) \approx 0.6$, the SDSS luminosity function then gives $L_B^* = 9.7 \times 10^9 \ h^{-2} \ L_{\odot,B}$, $\phi^* = 2.69 \times 10^{-2} \ h^3 \ Mpc^{-3}$ and $\alpha = -1.22$, while the 2dFGRS gives $L_B^* = 1.0 \times 10^{10} \ h^{-2} \ L_{\odot,B}$, $\phi^* = 1.69 \times 10^{-2} \ h^3 \ Mpc^{-3}$ and $\alpha = -1.28$. The predicted numbers of galaxies in this volume are ≈ 0.1 for both the SDSS and 2dFGRS luminosity functions. If L_B^* is increased by a factor of 2.7 or 3.2 for the SDSS and 2dFGRS luminosity functions, respectively, then nine galaxies are predicted. Because of the small comoving volumes enclosed in this redshift range, these numbers may not be indicative of the galaxy population as a whole. Furthermore, random errors in the photometric redshifts will tend to produce a bias in the derived luminosities, since the luminosity function declines very steeply toward higher luminosities, and the smoothing will increase the number of observed very luminous galaxies. We estimate this effect by convolving the Schechter function with a Gaussian of width 0.3 mag, characteristic of our errors. As a result, the required increase in L^* decreases to 2.4–2.9 with respect to locally determined values. It is clear that spectroscopic confirmation of the photometric redshifts of these bright galaxies is desirable.

Another striking feature is the lack of galaxies with $L_V^{rest} \gtrsim 1.4 \times 10^{10} \ h^{-2} \ L_{\odot}$ and $1.5 < z < 2$. Given the observed redshift structure in our field, this may simply be due to clustering. It is interesting, however, to note that Dickinson (2001b) found a similar paucity of intrinsically luminous galaxies at $1.4 < z < 2$ in the HDF-N. The photometric redshifts in this regime are particularly uncertain, however, since spectroscopic redshifts are rarely available. The derived z_{phot} between $1.5 < z < 2.5$ is very sensitive to the U-band photometry, since the LB moves into the U band. We tested how z_{phot} changes if the U-band data is omitted. The largest changes occur for galaxies with $2 < z < 2.5$, and their newly derived z_{phot} values are systematically lower. This suggests that z_{phot} might be biased if the bluest band falls just above the rest-frame LB.

5. SUMMARY AND CONCLUSIONS

We have presented the initial results from FIRES obtained with ISAAC at the VLT. We assembled a K_s-

band–selected catalog of galaxies in the HDF-S from the deepest NIR data taken of this field. Our catalog consists of 136 galaxies with $K_{s,AB} \leq 23.5$ and photometry in seven bands from 0.3 to 2.2 μm. Our unique combination of ultradeep optical data from *HST* with our deep NIR data allows us to sample the rest-frame V band in galaxies for $z \leq 3$ and to select galaxies in a way less dependent on the current SFR than the rest-frame UV.

To interpret these data, we have developed a new photometric redshift algorithm, which models the galaxy colors with a linear combination of empirical templates, and in so doing, makes minimal a priori assumptions about the galaxies' SFHs. Testing our method on galaxies with spectroscopic redshifts from the HDF-N and HDF-S, we find that our technique is precise and robust for all $z_{spec} < 6$ having a mean $\Delta z \approx 0.10$ for $z \leq 1.5$ and $\Delta z \approx 0.44$ for $z > 1.5$, with catastrophic errors in $\lesssim 3\%$ of the sample. The results from the HDF-S also confirm that our photometry is adequate for good z_{phot} estimates. We find that in almost all cases our best-fit SEDs match the observed fluxes well.

We developed a Monte Carlo code to estimate the uncertainty in z_{phot} arising from the flux errors. In agreement with previous work by other groups, we found that the uncertainty in z_{phot} is dominated at the faint end by photometric uncertainty and at the bright end by template mismatch. For bright galaxies, where spectroscopic redshifts are available, the uncertainty in z_{phot} is severely underestimated when it is derived solely from the flux uncertainties, although large values of δz_{MC} can help identify catastrophic errors in z_{phot}. To provide realistic, individual estimates on the accuracy of each galaxy's z_{phot}, we added our Monte Carlo errors in quadrature with the mean disagreement with z_{spec} as measured from the HDF-N and also flag galaxies with secondary minima in their $\chi^2(z)$ profiles.

Although the redshift is primarily constrained by the high signal-to-noise ratio *HST* optical data, the deep NIR data can break degeneracies between different template combinations at different redshifts, which have identical $V - I$ colors. While the NIR data greatly improves the redshift estimation at $z < 1.5$, it can actually worsen the z_{phot} estimate at high redshifts by causing the misidentification of a LB as a rest-frame optical break. The effect of the NIR should become increasingly important when the signal-to-noise ratio is dramatically improved, such as in the very deep exposures planned for FIRES. By fixing the position of rest-frame optical breaks at $z > 1$, our NIR data also allows us to probe the redshift distribution of all galaxy types at these epochs. We use our photometric redshift technique to estimate z_{phot} and its accompanying uncertainty for our entire K_s-band–selected sample.

Applying these techniques, we have found a sharp peak in the redshift distribution at $z \approx 0.5$ and a broad peak at $1 \leq z_{phot} \leq 1.4$. The $z \approx 0.5$ spike was first noticed by G01 using spectroscopic redshifts obtained with the AAT.

To compare our redshift distribution with the predictions of hierarchical galaxy formation models, we measured the fraction of galaxies at $z > 2$ in a $K_{s,vega} < 21$ sample to be 12%. We find that this fraction is much greater than that predicted by KC98 and F99 for a CDM universe with $\Omega_m = 1$, although it is in better agreement with a ΛCDM model. At all redshifts, we find far fewer bright galaxies than predicted by PLE models. We also find, however, that different groups working with similar data sets find different fractions of galaxies above a certain redshift threshold. This

disagreement stems from differences in z_{phot} determinations between groups.

Taking advantage of our extended wavelength coverage, we measure the rest-frame luminosity L^{rest} in the U, B, and V bands for the galaxies in our sample, regardless of their redshift. Many high-redshift galaxies have $L^{rest} \geq 5 \times 10^{10}$ $h^{-2} L_\odot$ in all bands, however, we find a paucity of galaxies with $L_V^{rest} \geq 1.4 \times 10^{10}$ $h^{-2} L_\odot$ between $1.5 < z < 2$. A similar deficit in the redshift distribution of intrinsically luminous galaxies was noted by Dickinson (2001b) using NICMOS data on the HDF-N. However, the photometric redshifts in this regime are uncertain, and spectroscopic confirmation of this deficit is required. At higher redshifts, the densities increase, and we find nine galaxies with $L_B^{rest} \geq 5 \times 10^{10}$ $h^{-2} L_{\odot,B}$ that lie between $2 \leq z \leq 3.5$. These numbers can be accounted for if L^* in the B band increases by a factor of 2.7–3.2 with respect to SDSS and 2dFGRS values. When accounting for uncertainties in the rest-frame luminosity, the required increase is 2.4–2.9. The redshifts and nature of these intrinsically bright galaxies at high z needs to be verified with spectroscopic follow-up.

It is tempting to associate the increase in the number density of bright galaxies at $z < 1.5$ compared to $1.5 < z < 2$ with the onset of disk formation. Spectroscopic studies of larger volumes are necessary to rule out that cosmic variance, or uncertainties in the photometric redshifts may dominate this effect.

REFERENCES

Adelberger, K. L., & Steidel, C. C. 2000, ApJ, 544, 218
Benítez, N. 2000, ApJ, 536, 571
Bertin, E., & Arnouts, S. 1996, A&AS, 117, 393
Bessell, M. S., & Brett, J. M. 1988, PASP, 100, 1134
Blanton, M. R., et al. 2001, AJ, 121, 2358
Brinchmann, J., & Ellis, R. S. 2000, ApJ, 536, L77
Bruzual A., G., & Charlot, S. 2001, in preparation
Casertano, S., et al. 2000, AJ, 120, 2747
Cohen, J. G., Cowie, L. L., Hogg, D. W., Songaila, A., Blandford, R., Hu, E. M., & Shopbell, P. 1996, ApJ, 471, L5
Cohen, J. G., Hogg, D. W., Blandford, R., Cowie, L. L., Hu, E., Songaila, A., Shopbell, P., & Richberg, K. 2000, ApJ, 538, 29
Coleman, G. D., Wu, C.-C., & Weedman, D. W. 1980, ApJS, 43, 393 (CWW80)
Connolly, A. J., Csabai, I., Szalay, A. S., Koo, D. C., Kron, R. G., & Munn, J. A. 1995, AJ, 110, 2655
Cox, A. N. 2000, Allen's Astrophysical Quantities (4th ed.; New York: Springer)
Cristiani, S., et al. 2000, A&A, 359, 489
Csabai, I., Connolly, A. J., Szalay, A. S., & Budavári, T. 2000, AJ, 119, 69
da Costa, L., et al. 2001, A&A, submitted
Dickinson, M., 2001a, in preparation
———. 2001b, in Building Galaxies: From the Primordial Universe to the Present, ed. F. Hammer, T. X. Thuan, T. V. Cayatte, B. Guideroni, & J. Trânh Than Vân (Gif-sur-Yvette: Ed. Frontières), 257
Fernández-Soto, A., Lanzetta, K. M., Chen, H.-W., Pascarelle, S. M., Yahata N. 2001, ApJS, 135, 41 (FS01)
Fernández-Soto, A., Lanzetta, K. M., & Yahil, A. 1999, ApJ, 513, 34 (FLY99)
Folkes, S., et al. 1999, MNRAS, 308, 459
Fontana, A., D'Odorico, S., Poli, F., Giallongo, E., Arnouts, S., Cristiani, S., Moorwood, A., & Saracco, P. 2000, AJ, 120, 2206
Fontana, A., Menci, N., D'Odorico, S., Giallongo, E., Poli, F., Cristiani, S., Moorwood, A., & Saracco, P. 1999, MNRAS, 310, L27 (F99)
Franx, M., et al. 2000, Messenger, 99, 20
Giallongo, E., D'Odorico, S., Fontana, A., Cristiani, S., Egami, E., Hu, E., & McMahon, R. G. 1998, AJ, 115, 2169
Giallongo, E., Menci, N., Poli, F., D'Odorico, S., & Fontana, A. 2000, ApJ, 530, L73

Glazebrook, K. 2001, in preparation (G01)
Gwyn, S. D. J., & Hartwick, F. D. A. 1996, ApJ, 468, L77
Kauffmann, G., & Charlot, S. 1998, MNRAS, 297, L23 (KC98)
Kinney, A. L., Calzetti, D., Bohlin, R. C., McQuade, K., Storchi-Bergmann, T., & Schmitt, H. R. 1996, ApJ, 467, 38
Kron, R. G. 1980, ApJS, 43, 305
Labbé, I., et al. 2001, in preparation
Lilly, S., et al. 1998, ApJ, 500, 75
Lilly, S. J., Le Fevre, O., Hammer, F., & Crampton, D. 1996, ApJ, 460, L1
Madau, P. 1995, ApJ, 441, 18
Madau, P., Ferguson, H. C., Dickinson, M. E., Giavalisco, M., Steidel, C. C., & Fruchter, A. 1996, MNRAS, 283, 1388
Mobasher, B., & Mazzei, P. 2000, A&A, 363, 517
Moorwood, A. F. 1997, Proc. SPIE, 2871, 1146
Papovich, C., Dickinson, M., & Ferguson, H. 2001, ApJ, in press
Pascarelle, S. M., Lanzetta, K. M., & Fernández-Soto, A. 1998, ApJ, 508, L1
Persson, S. E., Murphy, D. C., Krzeminski, W., Roth, M., & Rieke, M. J. 1998, AJ, 116, 2475
Poli, F., Giallongo, E., Menci, N., D'Odorico, S., & Fontana, A. 1999, ApJ, 527, 662
Pozzetti, L., Bruzual A., G., & Zamorani, G. 1996, MNRAS, 281, 953
Rigopoulou, D., et al. 2000, ApJ, 537, L85
Sawicki, M. J., Lin, H., & Yee, H. K. C. 1997, AJ, 113, 1
Schade, D., Lilly, S. J., Le Fevre, O., Hammer, F., & Crampton, D. 1996, ApJ, 464, 79
Steidel, C. C., Adelberger, K. L., Giavalisco, M., Dickinson, M., & Pettini, M. 1999, ApJ, 519, 1
Steidel, C. C., Giavalisco, M., Pettini, M., Dickinson, M., & Adelberger, K. L. 1996, ApJ, 462, L17
Steidel, C. C., & Hamilton, D. 1992, AJ, 104, 941
Thompson, R. I., Weymann, R. J., & Storrie-Lombardi, L. J. 2001, ApJ, 546, 694
Weymann, R. J., Storrie-Lombardi, L. J., Sawicki, M., & Brunner, R. J., ed. 1999, ASP Conf. Ser. 191, Photometric Redshifts and High Redshift Galaxies (San Francisco: ASP)
Williams, R. E., et al. 1996, AJ, 112, 1335